

1 **Comparison of hourly surface downwelling solar radiation estimated from MSG/SEVIRI and**
2 **forecast by RAMS model with pyranometers over Italy**

3

4 Stefano Federico¹, Rosa Claudia Torcasio², Paolo Sanò¹, Daniele Casella¹, Monica Campanelli¹, Jan
5 Fokke Meirink³, PingWang³, Stefania Vergari⁴, Henri Diémoz⁵, Stefano Dietrich¹

6 (1) ISAC-CNR, via del Fosso del Cavaliere 100, 00133 Rome, Italy

7 (2) ISAC-CNR, zona Industriale comparto 15, 88046 Lamezia Terme, Italy

8 (3) Royal Netherlands Meteorological Institute (KNMI), Utrechtseweg 297, De Bilt, The
9 Netherlands

10 (4) Technical Centre for Meteorology (CTM), ITAF, Italy

11 (5) ARPA Valle D'Aosta, Italy

12

13

14

ABSTRACT

15 In this paper, we evaluate the performance of two Global Horizontal solar Irradiance (GHI)
16 estimates, one derived from Meteosat Second Generation (MSG) and another from the one-day
17 forecast of the Regional Atmospheric Modeling System (RAMS) mesoscale model. The horizontal
18 resolution of the MSG-GHI is 3*5 km² over Italy, which is the focus area of this study. For this
19 paper, RAMS has the horizontal resolution of 4km.

20 The performance of MSG-GHI estimate and RAMS-GHI one-day forecast are evaluated for one
21 year (1 June 2013 – 31 May 2014) against data of twelve ground based pyranometers over Italy
22 spanning a range of climatic conditions, i.e. from maritime Mediterranean to Alpine climate.

23 Statistics for hourly GHI and daily integrated GHI are presented for the four seasons and the whole
24 year for all the measurement sites. Different sky conditions are considered in the analysis.

25 Results for hourly data show an evident dependence on the sky conditions, with the Root Mean
26 Square Error (RMSE) increasing from clear to cloudy conditions. The RMSE is substantially higher
27 for Alpine stations in all the seasons, mainly because of the increase of the cloud coverage for these
28 stations, which is not well represented at the satellite and model resolutions.

29 Considering the yearly statistics computed from hourly data for the RAMS model, the RMSE
30 ranges from 152 W/m² (31%) obtained for Cozzo Spadaro, a maritime station, to 287 W/m² (82%)
31 for Aosta, an Alpine site. Considering the yearly statistics computed from hourly data for MSG-
32 GHI, the minimum RMSE is for Cozzo Spadaro (71 W/m², 14%), while the maximum is for Aosta
33 (181 W/m², 51%). The Mean Bias Error (MBE) shows the tendency of RAMS to over forecast the
34 GHI, while no specific behaviour is found for MSG-GHI.

35 Results for daily integrated GHI show lower RMSE compared to hourly GHI evaluation for both
36 RAMS-GHI one-day forecast and MSG-GHI estimate. Considering the yearly evaluation, the
37 RMSE of daily integrated GHI is at least 9% lower (in percentage units, from 31% to 22% for
38 RAMS in Cozzo Spadaro) than the RMSE computed for hourly data for each station. A partial
39 compensation of underestimation and overestimation of the GHI contributes to the RMSE
40 reduction. Furthermore, a post-processing technique, namely Model Output Statistics (MOS), is
41 applied to improve the GHI forecast at hourly and daily temporal scales. The application of MOS
42 shows an improvement of RAMS-GHI forecast, which depends on the site considered, while the
43 impact of MOS on MSG-GHI RMSE is small.

44

45 **1. Introduction**

46 The Global Horizontal Irradiance (GHI) is the power of the solar spectrum reaching the surface and
47 it is a key parameter for several disciplines. In particular, the exploitation of solar energy, which is
48 the most abundant renewable energy, is of great interest because the larger penetration of renewable
49 energies into the energy market would reduce the emissions of greenhouse gases (Szuromi et al
50 2007; IEA, 2010; EWEA, 2011) caused by human activities.

51 Photovoltaic (PV) systems enable the conversion of the solar radiation into electricity through semi-
52 conductor devices and, in order to control the increase of global temperature, PV systems are
53 expected to have a potential by more than 200 GW by 2020 (EWEA, 2011).

54 For the operation and implementation of PV systems, observation and forecast of GHI play a major
55 role. Surface weather stations equipped with a pyranometer give reliable observations of GHI, but
56 they are often unavailable in the places where new installations are planned. For this purpose, the
57 GHI may be derived from other sources, as the Meteosat Second Generation (MSG) Spinning
58 Enhanced Visible and Infrared Imager (SEVIRI) or a Numerical Weather Prediction Model (NWP).

59 In this paper, we show the performance of both the MSG-GHI estimate, following the methodology
60 of Greuell et al. (2013), and RAMS-GHI one-day forecast over the whole Italian territory. To verify
61 GHI, we use twelve pyranometers, which are representative of sites with very different climates,
62 from Mediterranean maritime to Alpine. Moreover, the study spans a whole year to properly
63 account for the natural variability of the Mediterranean climate.

64 Many studies are available on the performance of different approaches to estimate and forecast solar
65 radiation in several countries in Europe (Roebeling et al, 2008; Greuell et al, 2013; Lara-Fanego et
66 al., 2012; Kosmopoulos et al., 2015; Gómez et al., 2016; Lorenz et al, 2009; Perez et al, 2006;
67 Rincon et al, 2011), because the planning of new PV systems and the managing of the electricity

68 grid with large amounts of production from solar energy requires the knowledge and forecast of
69 GHI with high accuracy. This study goes in this direction by considering a nation-wide evaluation
70 for a whole year. Moreover, Italy has a great potential for the exploitation of solar energy (Petrarca
71 et al., 2000).

72 We consider both the hourly and daily integrated GHI, the latter being the GHI integrated for each
73 day for the different datasets, to evaluate the performance of both RAMS-GHI and MSG-GHI for
74 two different timescales of interest. Also, we show the impact of a simple post processing
75 technique, which aims to reduce the Mean Bias Error (MBE) for each site, on the GHI estimate and
76 forecast.

77 The paper is organized as follows: Section 2 shows the datasets used and the methodology adopted
78 to evaluate the errors of the MSG-GHI estimate and RAMS-GHI one-day forecast; Section 3 shows
79 the results considering both the hourly and daily integrated GHI; Conclusions are given in Section
80 4.

81

82 **2. Data and methods**

83

84 *2.1 Cloud properties and GHI from MSG-SEVIRI*

85 The SEVIRI instrument onboard MSG carries 11 channels in the visible to infrared spectral range
86 with a spatial resolution of $3 \times 3 \text{ km}^2$ at the sub-satellite point and a temporal repeat frequency of 15
87 minutes. Over Italy the spatial resolution is about $3 \times 5 \text{ km}^2$. From the SEVIRI measurements, a
88 range of cloud physical properties can be derived with the Cloud Physical Properties (CPP)
89 algorithm. The algorithm first identifies cloudy and cloud contaminated pixels using a series of
90 thresholds and spatial coherence tests on the measured visible and infrared radiances (Roebeling et
91 al., 2008). Depending on the tests, the sky can be classified as clear, contaminated or overcast.
92 Subsequently, cloud optical properties (optical thickness) are retrieved by matching observed
93 reflectances at visible ($0.6 \mu\text{m}$) and near-infrared ($1.6 \mu\text{m}$) wavelengths to simulated reflectances of
94 homogeneous clouds composed of either liquid or ice particles. A
95 mixture of ice and water is not possible in this framework. The thermodynamic phase (liquid or ice)
96 is determined as part of this procedure, using a cloud-top temperature estimate as additional input
97 (Roebeling et al., 2008; Stengel et al., 2014).

98 Building on the retrieval of cloud physical properties, the Surface Insolation under Clear and
99 Cloudy Skies (SICCS) was developed to estimate surface downwelling solar radiation using broad-

100 band radiative transfer simulations (Deneke et al., 2008; Greuell et al., 2013). Both global
101 irradiance as well as the direct and diffuse components are retrieved. While the cloud properties are
102 the main input for cloudy and cloud-contaminated pixels, information about atmospheric aerosol
103 from the Monitoring Atmospheric Composition and Climate (MACC) project is used for cloud-free
104 scenes. The retrieval of cloud properties can be associated with large uncertainties, in particular due
105 to horizontal inhomogeneity (e.g., Coakley et al., 2005). However, subsequently derived irradiances
106 (such as SICCS GHI) have relatively much smaller uncertainty due to compensation of errors in
107 forward and inverse radiative transfer calculations (Greuell et al., 2013; see also Kato et al., 2006).
108 Uncertainties in MACC reanalysed aerosol properties contribute to errors in retrieved clear-sky GHI
109 but these errors are considerably smaller than those for cloudy skies (Greuell et al., 2013).

110 Greuell et al. (2013) performed an extensive validation of the MSG-SICCS retrievals with Baseline
111 Surface Radiation Network (BSRN) ground-based observations in Europe for the year 2006. They
112 found median values of the station GHI biases of $+7 \text{ W/m}^2$ (+2%) and hourly GHI RMSEs of 65
113 W/m^2 (18%).

114 The CPP and SICCS products are publicly available at msgcpp.knmi.nl.

115

116 *2.2 The RAMS set-up*

117 In this paper, we evaluate the performance of the RAMS-GHI one-day forecast. RAMS is a general
118 purpose limited area model designed to be used at the mesoscale (horizontal grid spacing ≈ 1 -100
119 km) or higher horizontal resolutions. It is based on a full set of non-hydrostatic, compressible
120 equations of the atmospheric dynamics and thermodynamics, plus conservation equations for scalar
121 quantities such as water vapour and liquid and ice hydrometeor mixing ratios. The model is widely
122 used for research as well as for weather forecast (Cotton et al., 2003).

123 The model is run with two one-way nested grids (Table 1, Figure 1). The coarser domain has 12 km
124 horizontal resolution and covers Central Europe, while the second domain has 4 km horizontal
125 resolution and covers the Italian peninsula. Thirty-six vertical levels, extending up to the lower
126 stratosphere, are used in the terrain-following coordinate system of RAMS.

127 The exchange between the atmosphere, the surface and the soil is computed by the LEAF (Land
128 Ecosystem-Atmosphere Feedback) submodel. The LEAF submodel considers the interaction among
129 several features, as well as their influence on the atmosphere: vegetation, soil, lakes and oceans, and
130 snow cover.

131 RAMS parameterises the unresolved transport using K -theory, in which the covariance is evaluated
132 as the product of an eddy mixing coefficient and the gradient of the transported quantity. The
133 turbulent mixing in the horizontal directions relates the mixing coefficients to the fluid strain rate
134 (Smagorinsky, 1963) and includes corrections for the influence of the Brunt-Vaisala frequency and
135 the Richardson number (Pielke, 2002).

136 Convective precipitation is parameterised following Molinari and Corsetti (1985), who modified the
137 Kuo scheme (Kuo, 1974) to account for downdrafts. The convective scheme is applied to the
138 coarser RAMS domain, while convection is assumed explicitly resolved for the inner domain.

139 Explicitly resolved precipitation is computed by the WRF (Weather Research and Forecasting
140 System) – single-moment-microphysics class 6 (WSM6) scheme (Hong et al., 2006), which was
141 recently adapted to RAMS (Federico, 2016).

142 Short wave and long wave radiation is computed by the Chen and Cotton scheme (Chen and Cotton,
143 1983); the radiative scheme accounts for the total condensate in the atmosphere but not for the
144 specific hydrometeor type. In particular, the scheme uses an “effective emissivity” for cloud layers,
145 where the cloud emissivity is parametrized empirically from observations (Stephens 1978). The
146 “effective emissivity” is a function of the total condensate water path, computed summing all
147 hydrometeors mixing ratios for each model level (liquid, i.e. cloud and rain, solid, i.e. ice and snow,
148 and mixed phase, i. e. graupel) and integrating over the cloud-layer (Chen and Cotton, 1983).

149 Initial and boundary conditions are interpolated from the operational analysis/forecast cycle issued
150 at 12:00 UTC by the ECMWF (European Centre for Medium range Weather Forecast). Initial and
151 boundary conditions are available at 0.5° horizontal resolution and on nine pressure levels, from
152 1000 to 30 hPa. No additional data are assimilated into the RAMS model.

153 The model was run for a whole year (1 June 2013 - 31 May 2014) with the above configuration and
154 with no hydrometeors at the initial time, with the exception of water vapour (cold start). Previous
155 unpublished studies with RAMS showed that 12 h are enough for the model to reach a dynamical
156 equilibrium between the dynamic, thermodynamic and cloud-precipitation fields starting from a
157 cold start. For this reason, each simulation lasts 36 h, starts at 12 UTC of the day before the day of
158 interest, and the first 12 h are used as spin-up time and discarded. The model output is available
159 hourly.

160

161 *2.3 Surface observations*

162 In this work, we consider 12 pyranometers over Italy (Figure 2). Their coordinates, height above the
163 sea level, the Institution responsible for their management, and abbreviations used in this paper are
164 shown in Table 2. The pyranometers span a wide range of climatic conditions: Trapani, Cozzo
165 Spadaro, Santa Maria di Leuca, Capo Palinuro, Pratica di Mare, Cervia, Pisa and Trieste are located
166 by the sea, and show a typical Mediterranean climate; Vigna di Valle is characterized by a mild
167 Mediterranean climate but it is located in more complex hilly terrain; Paganella, Monte Cimone and
168 Aosta are mountainous stations, and this has an important impact on the RAMS and MSG
169 performance at the sites. More specifically, Paganella is on the Alps, Monte Cimone is on the
170 Apennines, while Aosta, while at lower altitude, is embedded in the rough Alpine terrain.

171 The pyranometers are managed by two different institutions. The Aosta pyranometer is managed by
172 Arpa Valle D'Aosta, while all other pyranometers are managed by the Italian Air Force
173 (Aeronautica Militare). Each institution is responsible for its own measurements.

174 For pyranometers managed by the Italian Air Force, in addition to basic maintenance and installing
175 procedures recommended by WMO – Guide nr. 8, data quality is controlled following an internal
176 control procedure described in Vergari et al. (2010).

177 In particular, to improve quality control checks for global solar radiation and sunshine duration
178 data (available simultaneously for all stations of this paper managed by Aeronautica Militare), two
179 procedures have been implemented. A range limit check, applied to both variables separately,
180 concerns the respect of variables' physical limits. This check has been improved varying physical
181 limits in agreement to the latitude and the season. Furthermore, the monthly atmospheric clearness
182 index has been calculated from the climatic history of each site, by applying the linear form of the
183 Angstrom-Prescott model. Then, an upper and a lower bound for the solar radiation are defined as
184 linear functions of clearness index and the sunshine duration value. These bounds delimit the range
185 of the daily solar radiation.

186 Analyzing the distance of daily values from their bounds, it is also possible to prevent instrumental
187 electronic drifts. In fact, if this distance changes in an appreciable way, a recalibration procedure is
188 activated and the device is recalibrated by comparison with a standard pyranometer using the sun as
189 a source, under natural conditions of exposure (ISO ,1993). The reference standard used in this case
190 is a CM11 Kipp and Zonen, calibrated every two year by the WMO Regional Instrument Centre
191 Radiation of Carpentras (France), by comparison with a pyreliometer PMO6 and a pyranometer
192 CMP21.

193 For the Aosta pyranometer, in addition to the manual maintenance related to the periodical cleaning
194 of the dome, irradiance measurements are daily checked through comparison with clear-sky

195 simulations by a radiative transfer model (libRadtran, Emde et al., 2016) to check for electric wiring
 196 faults. In particular, measurements higher than 200% of the daily maximum expected from
 197 libRadtran in clear-sky conditions are removed. The CMP21 radiometer is calibrated every two
 198 years at the Physikalisch-Meteorologisches Observatorium Davos/World Radiation Center
 199 (PMOD/WRC) against a member of the World Standard Group (WSG) for the direct component
 200 and a shaded standard pyranometer of the World Radiation Center (WRC) for the diffuse
 201 component. The radiometric stability was better than 0.2% over the period of the six years of
 202 measurements.

203 Table 3 shows, for each station and season, as well as for the whole year, the percentage of data in
 204 clear, contaminated and overcast conditions, classified by the satellite method of Section 2.1.

205 There is a considerable variability of the sky conditions with the season for each station. For
 206 Trapani, for example, the percentage of clear sky in summer is 82%, while it reduces to 38% in fall
 207 and 48% in winter. Also, for each season, the variability of the sky conditions among the stations is
 208 high. For maritime stations, for example, the percentage of clear skies in summer is above 70% with
 209 few exceptions, while it reduces to 45, 34, 32% for Paganella, Monte Cimone and Aosta,
 210 respectively.

211

212 *2.4 Evaluation methodology*

213 The RAMS GHI forecast is available hourly, while the frequency of pyranometer observations and
 214 MSG-GHI estimate is every half an hour. Pyranometer observations and MSG-GHI estimates were
 215 considered hourly, at the same time of the RAMS forecast output. Starting from these data, the
 216 MBE (Mean Bias Error) and the RMSE (Root Mean Square Error) were computed:

$$217 \quad MBE = \frac{1}{N} \sum_{i=1}^N (x_{fi} - x_{oi}) \quad (1)$$

$$218 \quad RMSE = \sqrt{\frac{1}{N} \sum_{i=1}^N (x_{fi} - x_{oi})^2} \quad (2)$$

219 Where x_f is the RAMS forecast or the MSG GHI estimate, x_o is the pyranometer observation, and N
 220 is the total number of data available for the statistic.

221 In addition to the MBE and RMSE computed from hourly data, the statistics are computed starting
 222 from daily data. In this case, the integral of the GHI for the whole day is first computed for each
 223 dataset, then the MBE and RMSE are computed from the daily data.

224 Relative MBE and relative RMSE error measures (rMBE, rRMSE) are also used. The normalization
 225 is done with the pyranometer observation for the station and period considered, i.e. :

226

$$227 \quad rMBE = 100 \frac{\sum_{i=1}^N (x_{fi} - x_{oi})}{\sum_{i=1}^N x_{oi}} \quad (3)$$

$$228 \quad rRMSE = 100 \frac{\sqrt{\frac{1}{N} \sum_{i=1}^N (x_{fi} - x_{oi})^2}}{\frac{1}{N} \sum_{i=1}^N x_{oi}} \quad (4)$$

229 In order to improve the RAMS one-day hourly forecast and the MSG-GHI estimate, a post-
230 processing technique, namely the Model Output Statistics (MOS), is used. The MOS technique
231 improves the forecast/estimate of the GHI by reducing the MBE. The MBE is caused by several
232 factors related to both modelling and observations. In the context of this paper the most important
233 causes of MBE are: a) the approximations in the meteorological model and in the methodology used
234 to estimate GHI from MSG data, and; b) the horizontal grid used to represent the real world, which
235 smoothens the surface features causing systematic errors. Other contributions arise from small and
236 undetected systematic errors in the observations, and from the not exact simultaneity of the three
237 datasets (pyranometers, MSG-GHI, RAMS-GHI forecast).

238 The MOS used here consists of a linear regression computed between the GHI forecast (or estimate)
239 and observation for a training period:

$$240 \quad y = a + bx \quad (5)$$

241 where x is the RAMS-GHI one-day hourly forecast (or MSG hourly estimate) and y is the
242 pyranometer observation. The application of the MOS is described in Section 3.4.

243

244 **3. Results**

245 **3.1 General considerations on MSG estimate and RAMS forecast**

246 Figure 3a shows the scatter-plot of hourly GHI estimates of MSG and the corresponding
247 pyranometer observations for Vigna di Valle. The black dots refer to clear sky, while the red dots
248 are for contaminated and overcast conditions (after also referred to as cloudy conditions) for the
249 entire yearly dataset. Three regression curves are shown: the black one is for clear conditions, the
250 red one is for cloudy conditions (both contaminated and overcast) and the blue one is for the whole
251 dataset. Linear regression is computed using the pyranometer values as x and MSG-GHI forecast as
252 y . The parameters of the linear regressions are shown in the respective colours: a is the slope, b
253 is the intercept, r is the correlation coefficient, N is the number of data. The probability to have a
254 correlation coefficient larger than that found by chance is also shown ($p > r$). A small value of this
255 probability shows a high significance of the regression. The data for cloudy conditions of Figure 3a

256 show larger deviations from their regression line compared to clear sky data. This is confirmed by
257 the correlation coefficient, which is 0.96 for clear sky and 0.89 for contaminated and overcast
258 conditions. Also, the slope (intercept) of the linear regression is closer to 1.0 (closer to 0.0) for clear
259 sky, in better agreement with the perfect regression.

260 Considering Figure 3a, two types of error are evident: a) there are cases when the cloud
261 classification by MSG-GHI is wrong as, for example, for the black dots in the upper-left part of
262 Figure 3a. For these points, the MSG-GHI is high (larger than 600 W/m^2) while the pyranometer
263 observation is below 300 W/m^2 . This error becomes particularly important for mountainous stations
264 because, when the soil is covered by snow, it is more difficult for the MSG-GHI algorithm to
265 correctly identify the clouds; b) the correlation coefficient for cloudy conditions is lower compared
266 to clear sky data and shows the difficulty to correctly estimate the cloud optical depth, which can
267 result in both overestimation of the MSG-GHI, i.e. the cloud optical depth is underestimated, or
268 underestimation of the MSG-GHI, i.e. the cloud optical depth is overestimated. It is important to
269 note that red points may also contain cases of wrong cloud classification. Nevertheless, the larger
270 spread of the red points compared to the black ones shows, indirectly, the overall good
271 classification of the sky conditions by MSG because the estimation of the GHI is more difficult for
272 cloudy skies.

273 Figure 3b shows the scatter plot for the same station for the RAMS-GHI one-day hourly forecast.
274 Linear regression is computed using the pyranometer hourly values as x and corresponding RAMS-
275 GHI forecast as y . The RAMS-GHI forecast data show larger deviations from their regression line
276 compared to MSG-GHI. The correlation coefficient of the linear fit is 0.91 for clear conditions,
277 while it is 0.60 for contaminated and overcast sky, showing a rather poor performance of the
278 RAMS-GHI one-day hourly forecast in cloudy conditions. Both values are lower than the
279 corresponding values of the MSG-GHI estimate.

280 Figure 3b for clear sky shows cases when RAMS predicts clouds that are not observed, i.e. the
281 black dots in the lower right part of the figure, and cases when RAMS does not predict clouds that
282 are observed, i.e. the red dots in the upper-left part of the figure. Also, the large deviations of the
283 red dots from their regression line show either cases of incorrectly predicted sky conditions or
284 errors in the representation of the cloud optical depth.

285 From Figure 3 it follows that: a) the performance in clear conditions is better compared to cloudy
286 sky; b) the hourly estimate of the GHI by MSG outperforms the RAMS forecast. For the latter
287 point, however, it is emphasized that the MSG and RAMS performance cannot be directly

288 compared because RAMS is a forecast, while MSG is an estimate of the GHI from radiance
289 observations.

290 The results of Figure 3, even if shown for Vigna di Valle are found for all stations considered in this
291 paper, and are similar to the findings of several studies (Kosmopoulos et al., 2015; Lara-Fanego et
292 al., 2012; Gomez et al., 2016).

293 To show this point for other stations, Figure 4 shows the RMSE as a function of the cloud coverage
294 for MSG-GHI (Figure 4a) and for RAMS-GHI forecast (Figure 4b). In Figure 4a, the coloured bars
295 for each sky condition (1=clear, 2=contaminated and 3=overcast) show the GHI average computed
296 from the pyranometer hourly data, while the grey bars in the background show the RMSE of the
297 MSG-GHI estimate for the different sky conditions for hourly data.

298 Figure 4a shows that the GHI decreases for the sky changing from clear to cloudy conditions, while
299 the RMSE is higher when sky conditions become cloudier. More specifically, the RMSE is between
300 50 and 150 W/m^2 , depending on the station, for clear sky, between 50 and 200 W/m^2 for
301 contaminated conditions, and between 80 and 200 W/m^2 for overcast conditions.

302 Figure 4b shows the performance of the RAMS-GHI forecast as a function of the sky conditions.
303 The values of the pyranometers are the same as in Figure 4a and are shown to help comparison. The
304 RAMS-GHI one-day forecast RMSE increases from clear to overcast conditions and the error is
305 higher compared to MSG-GHI. More specifically, excluding mountainous stations, which have
306 larger errors, the RMSE is 100 W/m^2 for clear sky, 150-250 W/m^2 , depending on the station, for
307 contaminated sky, and around 250 W/m^2 for overcast conditions. In the latter case the RMSE is
308 larger than the GHI for most stations, i.e. the relative error is larger than 100%.

309 Because of the dependence of the MSG-GHI estimation and RAMS-GHI forecast on the sky
310 condition, a large variability of the performance is expected with the seasons and with the stations,
311 because the cloud coverage at each site varies with the season and, for each season, from site to site.
312 This point is investigated in the following sections.

313

314 **3.2 Performance dependence on the season and cloud cover**

315 Figure 5a shows the MBE of the MSG-GHI hourly estimate in all sky conditions for the different
316 seasons, for the whole year and for all stations. Focusing on the whole year, there are five stations
317 where the GHI is overestimated (maximum value at Monte Cimone; 18 W/m^2) and seven stations
318 where the GHI is underestimated (minimum value at Pratica Di Mare; -12 W/m^2). The MBE is,
319 however, small in absolute value and it is lower than 10 W/m^2 for seven pyranometers. Considering

320 the variability of the results with the station in all seasons, we note the larger absolute values for
321 mountainous stations. This is expected because there are a larger number of cloudy data for those
322 stations (Table 3) and the performance of the GHI estimate by MSG is worse for cloudy conditions
323 (Figure 3a). This result is general and applies also to the RAMS forecast.

324 Figure 5b shows the MBE for the RAMS-GHI one-day hourly forecast. Considering the statistics
325 for the whole year it is noted that the values are in general positive and below 30 W/m^2 , with the
326 exceptions of Paganella and Aosta where the MBE is negative, i.e. the RAMS forecast
327 underestimates the GHI, and reaches the huge value of -120 W/m^2 . The same behavior is found for
328 all seasons, with few exceptions. Excluding the mountainous stations of Aosta and Paganella, the
329 largest MBE is found in summer, showing the tendency of the RAMS forecast to overestimate the
330 GHI in this season, while the smallest values occur in spring. Considering the dependence of the
331 MBE with the station, it is evident the worse performance for mountainous stations, namely
332 Paganella and Aosta, compared to maritime stations. The inspection of the model output for those
333 stations reveals that the main source of error was the over forecast of cloudy conditions, as shown
334 by the scatter plots between the RAMS-GHI one-day hourly forecast and the corresponding
335 pyranometer values for these stations, given as a supplement to this paper. It is not easy to find the
336 reason for this behaviour, because several factors could be involved as errors in the physical and
337 numerical parameterizations of the model, and errors in the initial and boundary conditions. Also,
338 the 4 km horizontal resolution is not enough to resolve the fine orographic structures over the Alps
339 (Aosta and Paganella) and over the Apennines (Monte Cimone), and their interaction with the
340 atmosphere.

341 Figure 6a shows the RMSE for the MSG-GHI hourly estimate in all sky conditions for different
342 seasons, for the whole year and for the twelve stations. Considering the whole year, we note two
343 groups of stations: the first with values around 100 W/m^2 containing the maritime and hilly stations,
344 the second with values larger than 150 W/m^2 containing the mountainous stations. The increase of
345 the RMSE for mountainous stations is caused mainly by: a) the $3*5\text{km}^2$ horizontal resolution of the
346 MSG-GHI can be not enough to represent the local sky conditions at the pyranometer, especially for
347 mountainous stations where the complex orography determines rapid changes of the cloud coverage
348 in short distances; b) The classification of sky conditions is more difficult where the soil is covered
349 by snow and, because this condition is more frequent for mountainous stations, it increases the
350 MSG-GHI error for those stations; c) The estimate of the hourly GHI by the MSG is more difficult
351 in cloudy conditions (Figure 4), which are more frequent for mountainous stations. The different

352 performance of the two groups of stations is confirmed for all the seasons and highlights the
353 difficulty to clearly distinguish and classify clouds for the specific sites.

354 Considering the behavior of the RMSE with the season, the lowest values are often found in winter
355 even if the performance does not vary sizably with the season. Winter has also the lowest RMSE
356 averaged over all stations (84 W/m^2), followed by fall (98 W/m^2), summer (118 W/m^2), and spring
357 (125 W/m^2). The performance in winter is better compared to other seasons because the RMSE
358 statistic is sensitive to the larger errors (Wilks, 2006), and the departures of the GHI estimate from
359 the observation is lower in winter because the GHI is smaller. It is also noted the larger variability
360 of the performance in summer compared to other seasons, which will be discussed later on in this
361 section.

362 Another interesting statistic to quantify the performance of the MSG-GHI hourly estimate is the
363 rRMSE, which is shown in Table 4. Considering the whole year, this value ranges from 14% for
364 Cozzo Spadaro to 53% for Monte Cimone; for maritime and hilly stations the rRMSE is below
365 30%, while it is above 40% for mountainous stations, showing again the difference between the two
366 groups. The rRMSE has the smallest value in summer and the highest value in winter. While this
367 result is in part determined by the larger observed values of the GHI in summer, this analysis shows
368 more clearly the impact of the cloud coverage on the MSG-GHI performance. The percentage of
369 cloudy conditions is larger in winter compared to summer for all stations (Table 3) and the error of
370 the MSG-GHI is higher in cloudy conditions, as shown by the rRMSE. However, the larger
371 differences between the MSG-GHI hourly estimate and the pyranometer observation in summer,
372 even if in fewer occasions, determine larger values of the RMSE compared to winter, as shown in
373 Figure 6a.

374 Figure 6b shows the RMSE for the RAMS-GHI one-day hourly forecast. Considering the whole
375 year, the RMSE is below 200 W/m^2 for all stations with the exception of the mountainous stations,
376 where the error is larger because of the difficulty of the RAMS forecast to correctly predict the
377 cloud coverage. Considering the RMSE behavior for different seasons, averaged for all stations, the
378 lowest error is found in winter (142 W/m^2) followed by fall (171 W/m^2), summer (186 W/m^2) and
379 spring (245 W/m^2). Summer has the largest RMSE spread among the stations. In particular, it
380 shows the lowest error among all stations and seasons (Cozzo Spadaro, 110 W/m^2) but also values
381 larger than 300 W/m^2 for Paganella and Aosta. This result is caused by the large differences
382 between the RAMS-GHI one-day hourly forecast and observations. These differences are the
383 largest in summer (the lowest in winter) when the forecast of the cloud coverage is incorrect,

384 causing the largest (lowest) spread of the performance among stations. This applies also to the
385 MSG-GHI hourly estimate.

386 The RMSE of the RAMS-GHI one-day hourly forecast is more than twice that of the MSG-GHI
387 considering both the whole year and the seasons. The mountainous stations are an exception also in
388 this case because the performance of MSG and RAMS are closer. A better performance of the
389 MSG-GHI estimate is expected, because it is derived from the observations, while the RAMS is a
390 forecast, however the results of this section quantify the difference between the two GHI sources in
391 different conditions.

392 The rRMSE for the RAMS-GHI is shown in Table 5. Considering the yearly statistic, the values
393 range from 31% for Cozzo Spadaro to 81% for Aosta. The rRMSE varies considerably between the
394 mountainous stations compared to maritime and hilly stations, jumping from 53% obtained for
395 Trieste (the worst performance for maritime and hilly stations) to 72% of Paganella (the best
396 performance for mountainous stations). The variability of the rRMSE with the seasons shows again
397 the important impact of the cloud coverage on the RAMS-GHI one-day hourly forecast
398 performance. The smallest rRMSE are in summer, and the largest in winter for all stations.
399 Moreover, for Trieste, Cimone and Aosta the rRMSE is about 100 % or larger in winter.

400 Before concluding this section, it is interesting to compare the RAMS-GHI one-day hourly forecast
401 with the one-day hourly persistence forecast (Table 6). The one-day hourly persistence forecast
402 was computed using hour by hour the observed values of the previous day.

403 Considering the yearly statistics, the RAMS-GHI has a lower error compared to the one-day
404 persistence forecast for all pyranometer but Paganella. The improvement given by RAMS is larger
405 than 10% of the RMSE, showing a sizable impact. However, for Aosta, the difference between the
406 two forecasts is negligible.

407 Considering the performance of the RAMS-GHI and one-day persistence hourly forecasts with the
408 seasons, we note that: a) in winter the performance of the one-day persistence forecast is better than
409 the RAMS-GHI forecast for seven pyranometers. This result is obtained for six stations in fall, four
410 stations in spring and one station in summer; b) for mountainous stations the one-day persistence
411 hourly forecast is better than the RAMS-GHI one-day hourly forecast for most-cases. These results
412 show again the important impact of the cloud-coverage on the performance of the RAMS-GHI one-
413 day hourly forecast, nevertheless the RAMS forecast can give added valued to the GHI forecast in
414 most cases.

415

416

3.3 Daily evaluation and MOS application

417

In this section, we discuss the impact of the time interval on the RAMS-GHI and MSG-GHI performance.

418

419

Figure 7a shows the rRMSE for different stations and seasons for the RAMS-GHI one-day forecast.

420

This figure is still computed from hourly data, as in the previous section (Figure 4b), but the RMSE

421

is expressed in percentage to help comparison among statistics presented in this section.

422

Figure 7b shows the rRMSE for daily integrated GHI. Comparing the result of Figures 7a and 7b, it

423

is apparent the impact of the time interval on the rRMSE. Considering the yearly result, for

424

example, the rRMSE is reduced by more than 9% (in percentage units and the percentage is

425

computed respect to the corresponding observations, Eqn. (2) and Eqn. (3)) for all stations when the

426

statistics are computed for daily integrated GHI, and for several stations the improvement is larger

427

than 15%. This improvement is found for all seasons and stations. In addition to the way used to

428

compute the statistic, which produces smaller values compared to the same statistic for hourly data,

429

the improvement is also caused by a partial compensation of the forecast underestimation and

430

overestimation of the GHI during the day.

431

Considering the rRMSE for the MSG-GHI, a similar improvement is found, when computed for

432

daily integrated GHI (Table 4). For the yearly statistics, the rRMSE decreases by 10% or more for

433

all stations and an improvement larger than 5% is found in all seasons with a considerable variation

434

among the stations.

435

436

3.4 MOS application

437

The last problem considered in this paper is the impact of the Model Output Statistics (MOS) on the

438

one-day RAMS-GHI forecast and on the MSG-GHI, both for hourly and daily integrated GHI. The

439

MOS was computed for each season and the “leave one” methodology was used to verify the

440

RAMS forecast (MSG estimate) using MOS. This method is a cross-validation method to assess

441

how the MOS prediction will perform in practice. For each hour of a season, the dataset is divided

442

in two parts: a) the actual data (or actual value), which is the value at the selected hour of the

443

RAMS one-day hourly forecast (or the MSG hourly estimate of GHI) and the corresponding

444

pyranometer observation, and: b) the training dataset, which is composed by all data in the season

445

with the exception of the actual data. The Eqn. (5) is computed for the training dataset (y is the

446 pyranometer value and x is the RAMS one-day hourly forecast or MSG hourly estimate of GHI),
447 and it is applied to the actual data, which is the x , to give the corrected forecast (y). Because the
448 MOS is computed starting from hourly data, the training period is all the season but one hour. This
449 procedure was repeated for all the hourly data in the season, obtaining the time series of the
450 corrected RAMS one-day hourly forecast and of the corrected MSG hourly estimation of the GHI.
451 The RMSE and rRMSE were computed for the corrected forecast/estimate of the GHI. In this way,
452 the data used for computing MOS is statistically independent from the dataset used for the
453 verification.

454 The statistic computed from hourly data are shown in Table 6 for the RAMS forecast. It is apparent
455 that the MOS improves the RAMS performance especially for Aosta and Paganella, where the Bias
456 is high (Figure 5b). In particular, after the MOS application, the absolute value of the Bias is less
457 than 30 W/m^2 for Paganella and Aosta for all seasons as well as for the whole year (not shown).
458 With the MOS application, the RAMS-GHI one-day hourly forecast performs better than the one-
459 day persistence hourly forecast for all stations considering the whole year, even if there are still
460 occasions when the one-day persistence hourly forecast has a better performance than the RAMS-
461 GHI one-day hourly forecast (Paganella in winter and fall, Aosta in winter, spring and fall, Trapani
462 in winter).

463 Starting from hourly data after the MOS correction, daily integrated GHI statistics were also
464 computed. The rRMSE of RAMS-GHI one-day forecast is shown in Figure 7c and Table 5. The
465 rRMSE decreases by 2-8% (in percentage units) for most stations compared to the daily integrated
466 GHI without MOS, with exception of Paganella and Aosta, where the improvement is larger. This is
467 expected because the Bias is larger for these stations (Figure 5b) and the MOS is a technique that
468 improves the forecast by reducing the Bias. This is confirmed by the inspection of the rMBE (not
469 shown), which is reduced by the application of the MOS.

470 The application of the MOS to the MSG-GHI gives no improvement on both rRMSE (Table 4) and
471 rMBE (not shown). This is caused by the small values of the Bias of the MSG-GHI (Figure 5a).

472

473 **4. Summary and conclusions**

474 In this paper, we analyzed the performance of the MSG-GHI estimation and RAMS-GHI one-day
475 forecast for one year (1 June 2013 - 31 May 2014) over the Italian territory. Twelve pyranometers,
476 scattered over the country and representing a variety of climate characteristics, were used to

477 evaluate the performance. The analysis was performed for both hourly values and daily integrated
478 GHI, and the dependence with the season and sky conditions was studied.

479 The results for the analysis on hourly data show the dependence of the MSG-GHI estimation and
480 RAMS-GHI forecast on the sky conditions, which mirrors in a notable dependency with the season
481 and station. In particular, mountainous stations have worse performance compared to hilly and
482 maritime stations.

483 The analysis of the MBE for the RAMS-GHI shows that the one-day hourly forecast overestimates
484 the GHI, with the exception of the mountainous stations of Paganella and Aosta, where a
485 considerable underestimation is found. The MSG-GHI doesn't show a specific behavior of the MBE
486 with both overestimation and underestimation, depending on the season and station.

487 The RMSE for the RAMS-GHI one-day hourly forecast is the lowest in winter, followed by fall and
488 spring. In summer, the RMSE shows the largest difference among the stations, the maritime stations
489 showing the best performance, because the RMSE is sensitive to the departures between forecast
490 and observation, which are larger in summer when the cloud coverage is not well predicted or
491 estimated at the site.

492 The RMSE of the MSG-GHI hourly estimate is more than halved compared to RAMS-GHI, with
493 the exception of the mountainous stations where the RMSE of the two datasets are closer.

494 The cloud coverage has an important impact also on the RMSE of both MSG-GHI hourly estimate
495 and RAMS-GHI one-day hourly forecast. The error is higher for cloudy conditions compared to
496 clear sky. This is especially evident for RAMS because the RMSE averaged over all the stations
497 varies from 91 W/m², to 191 W/m², and to 245 W/m² for clear, contaminated and overcast
498 conditions, respectively; for MSG-GHI, the RMSE averaged over all stations varies from 68 W/m²,
499 to 123 W/m², and to 98 W/m² for clear, contaminated and overcast conditions, respectively.
500 However, the analysis of the rRMSE reveals more clearly the impact of the cloud coverage on the
501 performance. Both RAMS-GHI one-day hourly forecast and MSG-GHI hourly estimate show the
502 largest rRMSE in winter and the lowest in summer, following the behaviour of the cloud coverage.

503 The increase of the RMSE with the cloud coverage is a combination of both the inability of the two
504 methods to correctly represent the cloud coverage and of the difficulty to compute the GHI in
505 cloudy conditions.

506 The results for daily integrated GHI show a notable improvement of the RAMS-GHI and MSG-GHI
507 performance. The partial compensation of overestimation and underestimation during the day

508 improves the performance for the daily integrated GHI. This result is similarly shown in other
509 studies for different countries (Lara-Fanego et al., 2012; Kosmopoulos et al., 2015; Gómez et al.,
510 2016).

511 Applying a simple post-processing technique, i.e. the MOS, to the RAMS-GHI one-day hourly
512 forecast reduces the RMSE (2-8% of its value), while the MOS has a negligible impact on the
513 MSG-GHI RMSE.

514 The performance of the RAMS-GHI one-day hourly forecast, with and without the MOS correction,
515 has been compared with the one-day persistence hourly forecast to quantify the added value of the
516 RAMS forecast. The results show that the RAMS forecast, especially with the MOS correction,
517 outperforms the one-day persistence forecast and that the improvement is often larger than 10% of
518 the RMSE. Nevertheless, there are still few occasions (Paganella in winter and fall, Aosta in winter,
519 spring and fall, and Trapani in winter) when the one-day persistence forecast outperforms the
520 RAMS forecast.

521 The results of this paper are representative of the current operational implementation of the RAMS
522 model at ISAC-CNR. There have been recent improvements to the RAMS model (CSU-RAMS,
523 <http://vandenheever.atmos.colostate.edu/vdhp/rams.php>) that will be explored in future studies
524 to improve the GHI forecast. The errors of the RAMS forecast for the GHI can be divided in three,
525 non-exhaustive, main components: a) errors in the prediction of the cloud coverage; b) errors in the
526 simulation of the interaction between the radiation and the clouds; c) errors in the representation of
527 the aerosol effects on the GHI.

528 As shown by the results of this and others papers, the error (RMSE) on the prediction of the GHI is
529 of the order of the GHI when the cloud coverage is not well represented. Errors of both physical and
530 numerical parameterizations of the model, but also errors in the initial and boundary conditions
531 contribute to this issue. In particular, the microphysical scheme influences the whole simulation
532 through a multitude of dynamic, radiative, thermodynamic and microphysics processes. The WSM6
533 scheme used in this paper is a single-moment scheme, predicting the mixing ratios of six
534 hydrometeors (vapour, cloud, rain, graupel, ice, snow). The WSM6 gave better performance
535 compared to other single-moment microphysics schemes included in RAMS for twenty cases over
536 Italy characterized by widespread convection and, for this reason, it is used in the operational
537 implementation at ISAC-CNR. However, the inability of single-moment schemes to allow the
538 number concentration and mean diameter of hydrometeors to vary independently limits their ability
539 to simulate clouds with characteristics consistent with observations across a wide range of

540 atmospheric conditions. Also, the sensitivity of these schemes to fixed parameters as, for example,
541 the number concentration of the hydrometeors, is high (Igel et al., 2015).

542 When both the mixing-ratio and number concentration can be predicted, as in double-moment
543 schemes, the description of the physical processes as condensation, collision-coalescence, and
544 sedimentation is improved. For this reason, double-moment schemes outperform single-moment
545 schemes as shown in several studies (Igel et al., 2015 and references therein).

546 The CSU-RAMS model includes a double-moment microphysics scheme (Meyers et al., 1997) that
547 could improve the prediction of the cloud coverage and will be considered in future studies.

548 Also, the cumulus parameterization scheme has an important role on the NWP forecast, especially
549 for cloud prediction. In addition to the Kuo scheme, used in this paper for the first domain, RAMS
550 implements the Kain-Fritsch scheme (Castro et al., 2005). This scheme will be used in future
551 studies to assess the sensitivity of the performance to the choice of the cumulus parameterization
552 scheme.

553 Another important point to consider for improving the model performance of the GHI forecast is the
554 change in the optical properties of the clouds when the liquid and ice phases are considered in the
555 radiative scheme (Harrington et Olsson, 2001; Sun and Shine, 1995). The Chen and Cotton scheme
556 (Chen and Cotton, 1983) used in this paper, while fast and efficient from the computational point of
557 view, considers the total condensate in the atmosphere but not the phase of the water (i.e. ice, liquid
558 or mixed). Numerical and observational experiments (Harrington et Olsson, 2001; Sun and Shine,
559 1995) show that the impact of the water phase is significant for the computation of the GHI because
560 the absorption and emissions are largely reduced in ice compared to liquid path with the same water
561 path.

562 Finally, our radiative scheme neglects the impact of the aerosols. This impact, however, can be very
563 important. For example, Lara-Fanego et al. (2012) show that the overestimation of the GHI by WRF
564 over Andalusia in clear sky conditions was caused by the underestimation of the aerosol optical
565 depth (AOD), which was assumed 0.1 for their experiments. Zamora et al. (2005) showed that a
566 doubling of the AOD considered in the Dudhia scheme (Dudhia, 1989) was responsible for a
567 decrease of the GHI of about 100 W/m^2 at the solar noon over US. Kosmopoulos et al. (2017)
568 investigates the impact of an extremely high dust event (maximum AOD 3.5), occurred from 30
569 January to 3 February 2015 over Greece. For this event, they found an attenuation of the GHI up to
570 40-50 %. They also show that, for climatological conditions, the attenuation of the GHI by the
571 aerosol load is less than 10%. Considering the above results and the fact that the RMSE statistic

572 used in this paper is sensitive to large errors, an important impact of the aerosols is expected. The
573 Harrington et al. (1997) radiation scheme is aerosol sensitive, is available in CSU-RAMS, and will
574 be tested in future studies.

575 To put the results of this paper in a more general context, we compare our statistics with similar
576 studies in the Mediterranean area (Greece and Spain).

577 Kosmopoulos et al. (2015) quantified the performance of the MM5 model for the one- and two-days
578 forecast over Greece. The forecast was compared with eleven pyranometers displaced over the
579 country. The RMSE computed from hourly data and for the one-day forecast ranges between 160
580 W/m^2 for the Chania station to 230 W/m^2 for Amfiklia. The error increases with the terrain
581 complexity and cloud coverage: Chania is located in the western part of the Crete Island and shows
582 a Mediterranean climate, while Amfiklia is located in one of the highest plateaus of Greece,
583 bounded at the west by the Pindos mountain. The RMSE shows a small increase between the first
584 and second day of forecast. With the exception of the mountainous stations of this paper, where the
585 RMSE is larger, our performance is in line with that of Kosmopoulos et al. (2015). Also, both studies
586 show a positive MBE with values of few tens of W/m^2 for most stations, with the exception of
587 Paganella and Aosta stations of this study where the MBE is larger in absolute value.

588 Gómez et al. (2016) quantified the performance of the RAMS model (both versions 4.4 and 6.0) for
589 the one-, two- and three-days GHI forecast over the Valencia Region. They considered thirteen
590 pyranometers widespread over the region. Focusing on the RMSE for hourly data in summer, they
591 found errors of 200 W/m^2 for flat terrain and 250 W/m^2 for hilly terrain. The RMSE for winter is
592 150-160 W/m^2 , depending on the stations. The MBE is of few tens of W/m^2 and it is positive. They
593 found similar results among the three days of forecast and also between the two versions of the
594 RAMS model. With the exceptions of the mountainous stations of this paper, where both the RMSE
595 and MBE in absolute value are larger, our results are in line with those of Gómez et al. (2016).

596 Lara Fanego et al. (2012) examined the performance of the WRF model for the GHI one- two- and
597 three-days forecast over Andalucia (Spain). They consider four stations: Andasol, Jerez, Cordoba
598 and Huelva. The RMSE computed from hourly data for the whole year is 140 W/m^2 for Cordoba,
599 Jerez ad Huelva stations and 170 W/m^2 for Andasol. Differences of the RMSE among the three
600 days of forecast are small. The RMSE of Lara Fanego et al. (2012) is smaller (10-20 W/m^2) than
601 those of this paper. This result can be caused by the difference of the climate and orography at the
602 stations considered in the two studies, nevertheless a better treatment of the interaction between
603 aerosols and radiation in Lara Fanego et al. (2012) contribute to this difference. The MBE of Lara

604 Fanego et al (2012) is in line with that of this paper, with the exception of Paganella and Aosta
605 stations.

606 Overall, the results of this paper show that the MSG-GHI estimate and the RAMS forecast have still
607 big issues in cloudy conditions. In particular, considering the potential of the RAMS forecast to
608 participate to the energy market, it is difficult to assess its usefulness from the results of this paper.
609 While the RAMS forecast outperforms the one-day persistence forecast in clear sky, it has large
610 errors in cloudy conditions and it is not easy to give a final balance between the advantages in clear
611 conditions and disadvantages in cloudy conditions. Considering also the variability of the RAMS
612 performance from site to site, the usefulness of the RAMS forecast from an economic perspective
613 must be evaluated from case to case (Wittman et al. 2008).

614

615 **Acknowledgments**

616 The ECMWF and CNMCA (Centro Nazionale di Meteorologia e Climatologia Aeronautica) are
617 acknowledged for the use of the MARS (Meteorological Archive and Retrieval System). Two
618 anonymous reviewers and Stephen Saleeby are acknowledged for their comments that improved the
619 quality of the paper.

620

621 **References**

622 Castro, C. L., R. A. Pielke Sr., and G. Leoncini (2005), Dynamical downscaling: Assessment of
623 value retained and added using the Regional Atmospheric Modeling System (RAMS), *J. Geophys.*
624 *Res.*, 110, D05108, doi:10.1029/2004JD004721.

625 Chen C., Cotton W.R., “A One-Dimensional Simulation of the Stratocumulus-Capped Mixed
626 Layer”, *The Boundary Layer Meteorology*, 25, 289–321, 1983.

627 Coakley, J. A., M.A. Friedman, and W. R. Tahnk (2005), Retrieval of cloud properties for partly
628 cloudy imager pixels, *J. Atmos. Oceanic Technol.*, 22, 3–17.

629 Cotton W. R., Pielke R. A. Sr., Walko R. L., Lista D. E., Tremback C. J., Jiang H., McAnelly R. L.,
630 Harrington J. Y., Nicholls M. E., Carrio G. G., McFadden J. P., “RAMS 2001: Current status and
631 future directions”, *Meteorology and Atmospheric Physics*, 82, 5-29, 2003.

632 Deneke H. M., A.J. Feijt, and R.A. Roebeling, “Estimating Surface Solar Irradiance from
633 METEOSAT SEVIRI-derived Cloud Properties”, *Remote Sensing of Environment*, 112 (6), 3131-
634 3141, 2008.

635 Dudhia, J., 1989. Numerical study of convection observed during the winter monsoon experiment
636 using a mesoscale two-dimensional model. *J. Atmos. Sci.* 46, 3077–3107.

637 Emde, C., Buras-Schnell, R., Kylling, A., Mayer, B., Gasteiger, J., Hamann, U., Kylling, J., Richter,
638 B., Pause, C., Dowling, T., and Bugliaro, L.: The libRadtran software package for radiative transfer
639 calculations (version 2.0.1), *Geosci. Model Dev.*, 9, 1647-1672, doi:10.5194/gmd-9-1647-2016,
640 2016

641 EWEA, The European Wind Energy Association, “EU Energy Policy to 2050: achieving 80-95%
642 emissions reductions”, March 2011.

643 Federico S., “Implementation of the WSM5 and WSM6 Single Moment Microphysics Scheme into
644 the RAMS Model: Verification for the HyMeX-SOP1”, *Advances in Meteorology*, Volume 2016,
645 Article ID 5094126, 17 pages, 2006. <http://dx.doi.org/10.1155/2016/5094126>.

646 Gómez I., Caselles V., and Estrela M. J., “Seasonal Characterization of Solar Radiation Estimates
647 Obtained from a MSG-SEVIRI-Derived Dataset and a RAMS-Based Operational Forecasting
648 System over the Western Mediterranean Coast”, *Remote Sensing*, 8(1),46, 2016.
649 doi:10.3390/rs8010046

650 Greuell, W., Meirink J.F. and Wang P., “Retrieval and validation of global, direct, and diffuse
651 irradiance derived from SEVIRI satellite observations”, *Journal of Geophysical Research*, 118,
652 2340-2361, 2013. doi:10.1002/jgrd.50194 <<http://dx.doi.org/10.1002/jgrd.50194>>.

653 Harrington, J. Y., and P. Q. Olsson, 2001: A Method for the Parameterization of Cloud Optical
654 Properties in Bulk and Bin Microphysical Models: Implications for Arctic Cloudy Boundary
655 Layers. *Atmos. Res.*, **57**, 51-80.

656 Harrington, J. Y., 1997: The effects of radiative and microphysical processes on simulated warm
657 and transition season Arctic stratus. Ph.D. dissertation, Colorado State University, 289 pp.
658 [Available from Colorado State University, Dept. of Atmospheric Science, Ft. Collins, CO 80523.]

659 Hong S.Y. and Lim J.J.O., “The WRF single-moment 6-class microphysics scheme
660 (WSM6)”, *Journal of the Korean Meteorological Society*, vol. 42, pp. 129–151, 2006.

661 IEA, Electricity information, Published by the International Energy Agency, p. 762, 2010.

662 Igel, A.L., M.R. Igel, and S.C. van den Heever, 2015: Make It a Double? Sobering Results from
663 Simulations Using Single-Moment Microphysics Schemes. *J. Atmos. Sci.*, 72, 910–925, doi:
664 10.1175/JAS-D-14-0107.1.

665 ISO, 1993: Solar Energy – Calibration of a Pyranometer Using a Pyrheliometer, ISO 9846:1993.
666 Geneva.

667 Kato, S., L. M. Hinkelman, and A. Cheng (2006), Estimate of satellite-derived COT and effective
668 radius errors and their effect on computed domain-averaged irradiances, *J. Geophys. Res.*, 111,
669 D17201, doi:10.1029/2005JD006668.

670 Kosmopoulos, P. G., Kazadzis, S., Taylor, M., Athanasopoulou, E., Speyer, O., Raptis, P. I.,
671 Marinou, E., Proestakis, E., Solomos, S., Gerasopoulos, E., Amiridis, V., Bais, A., and Kontoes, C.:
672 Dust impact on surface solar irradiance assessed with model simulations, satellite observations and
673 ground-based measurements, *Atmos. Meas. Tech. Discuss.*, doi:10.5194/amt-2017-79, in review,
674 2017.

675 Kosmopoulos P.G., Kazadzis S., Lagouvardos K., Kotroni V., Bais A, “Solar energy prediction and
676 verification using operational model forecasts and ground-based solar measurements”,
677 *Energy*,93,1918-1930, 2015.

678 Kuo H. L., “Further Studies of the Parameterization of the Influence of Cumulus Convection on
679 Large-Scale Flow”, *Journal of Atmospheric Sciences*, 31, 1232–1240, 1974.

680 Lara-Fanego V., Ruiz-Arias J.A., Pozo-Vazquez D. , Santos-Alamillos F.J., Tovar-Pescador J.,
681 “Evaluation of the WRF model solar irradiance forecasts in Andalusia (southern Spain) ”, *Solar*
682 *Energy*,86, 2200–2217, 2012.

683 Lorenz E, Remund J, Muller C, Traunmuller W, Steinmaurer G, Pozo D, Ruiz-Arias J.A., Fanego
684 V.L., Ramirez L., Romeo M.G., Kurz C., Pomares L.M., Guerrero C., “Benchmarking of different
685 approaches to forecast solar irradiance”, *EUPVSEC proceedings*, p. 4199e208, 2009.
686 <http://dx.doi.org/10.4229/24thEUPVSEC2009-5BV.2.50>.

687 Meyers, M. P., R. L. Walko, J. Y. Harrington, and W. R. Cotton, 1997: New RAMS cloud
688 microphysics parameterization. Part II: The two-moment scheme. *Atmos. Res.*, 45, 3–39,
689 doi:10.1016/S0169-8095(97)00018-5.

690 Molinari J., and Corsetti T., “Incorporation of cloud-scale and mesoscale down-drafts into a
691 cumulus parametrization: results of one and three-dimensional integrations”, *Monthly Weather*
692 *Review*, 113, 485-501, 1985.

693 Perez R., Moore K., Wilcox S., Renne D., Zelenka A., “Forecasting solar radiation e preliminary
694 evaluation of an approach based upon the national forecast database”, *Solar Energy* 81,809-12,
695 2006.

696 Petrarca S., Cogliani E., Spinelli, F., “La radiazione solare globale al suolo in Italia” *Enea, Rome*,
697 193 pp, 2000.

698 Pielke R. A., “Mesoscale Meteorological Modeling”, *Academic Press, San Diego*, 676 pp, 2002.

699 Rincon A., Jorba O., Baldasano J.M., Della Monache L., “Assessment of short-term irradiance
700 forecasting based on post-processing tools applied on WRF meteorological simulations”, *ESI002:*
701 *Workshop*, March 22-23, 2011.

702 Roebeling R. A., Deneke H. M., and Feijt A. J., “Validation of cloud liquid water path retrievals
703 from SEVIRI using one year of CloudNET observations”, *Journal of Applied Meteorology and*
704 *Climatology*, 47, 206–222, 2008.

705 Smagorinsky J., “General circulation experiments with the primitive equations. Part I, The basic
706 experiment”, *Monthly Weather Review*, 91 (3), 99-164, 1963.

707 Stengel, M., Kniffka, A., Meirink, J.F., Lockhoff, M., Tan, J. & Hollmann, R. “CLAAS: the CM
708 SAF cloud property dataset using SEVIRI”. *Atmospheric Chemistry and Physics*. 14, 4297–4311 ,
709 2014.

710 Stephens, G. L.: 1978, ‘Radiation Profiles in Extended Water Clouds, Part II’, *J. Atmos. Sci.* 35,
711 2123-2132.

712 Sun, Z., Shine, K.P., 1995. Parameterization of ice cloud radiative properties and its application to
713 potential climatic importance of mixed-phase clouds. *J. Clim.* 8, 1874–1888.

714 Szuromi P., Jasny B., Clery D., Austin J., Hanson B., “Energy for the long haul”, *Science*, 315
715 (5813):781, 2007.

716 Vergari, Foti, Vuerich, Cucchiarelli and Iorio, 2010: Improvements of the quality control system for
717 solar radiation and sunshine duration data at the Centre of Meteorological Experimentations
718 (ReSMA) of the Italian Air Force National Met Service (INMS). TECO 2010, Helsinki, FINLAND.

719 Wilks, D. S., 2006. *Statistical Methods in the Atmospheric Sciences*, Academic Press, 627 pp.

720 Wittmann, M., Breitkreuz, H., Schroedter-Homscheidt, M., Eck, M., “Case-Studies on the Use of
721 Solar Irradiance Forecast for Optimized Operation Strategies of Solar Thermal Power Plants”. *IEEE*
722 *J. Selected Topics Appl. Earth Observations Remote Sens.* 1 (1), 18– 27, 2008.

723 WMO, *Guide to Meteorological Instruments and Methods of Observation: (CIMO guide)*, 2014,
724 1139 pp. Available at: https://library.wmo.int/opac/doc_num.php?explnum_id=3121 (last access 27
725 April 2017).

726 Zamora, R.J., Dutton, E.G., Trainer, M., McKeen, S.A., Wilczak, J.M., Hou, Y.T., 2005. The
727 accuracy of solar irradiance calculations used in mesoscale numerical weather prediction. *Mon.*
728 *Weather Rev.* 133, 783–792.

729

730

731 **Tables and Figures**

732 Table 1: RAMS grid-setting for the first and second grids. NNXP, NNYP and NNZP are the
 733 number of grid points in the west-east, north-south, and vertical directions. Lx(km), Ly(km), Lz(m)
 734 are the domain extensions in the west-east, north-south, and vertical directions. DX(km) and
 735 DY(km) are the horizontal grid resolutions in the west-east and north-south directions. CENTLON
 736 and CENTLAT are the geographical coordinates of the grid centres.

737

738

	First grid	Second grid
NNXP	231	401
NNYP	231	401
NNZP	36	36
Lx	2772 km	1600 km
Ly	2772 km	1600 km
Lz	≈22 km	≈22 km
DX	12 km	4 km
DY	12 km	4 km
CENTLAT (°)	42.0	42.0
CENTLON (°)	12.5	12.5

749

750 Table 2: Station names, abbreviations, coordinates, height above the sea level (meters, forth
 751 column), instrument type and managing institution for the twelve sites.

Station name	Abbreviation	Coordinates (lon;lat)	Height (m) a.s.l	Pyranometer type	Institution
Trapani	tra	12.5; 37.9	9	CM11 Kipp&Zonen	Aeronautica Militare
Cozzo Spadaro	csp	15.1; 36.7	51	CM11 Kipp&Zonen	Aeronautica Militare
Santa Maria di Leuca	sml	18.3; 39.8	112	CM11 Kipp&Zonen	Aeronautica Militare
Capo Palinuro	pal	15.3; 40.0	185	CM11 Kipp&Zonen	Aeronautica Militare
Pratica di Mare	pdm	12.5; 41.7	32	CM11 Kipp&Zonen	Aeronautica Militare

Vigna di Valle	vdv	12.2; 42.1	266	CM11 Kipp&Zonen	Aeronautica Militare
Pisa	pis	10.4; 43.7	6	CM11 Kipp&Zonen	Aeronautica Militare
Cervia	cer	12.3; 44.2	10	CM11 Kipp&Zonen	Aeronautica Militare
Trieste	tri	13.8; 45.7	4	CM11 Kipp&Zonen	Aeronautica Militare
Monte Cimone	cim	10.7; 44.2	2173	CM11 Kipp&Zonen	Aeronautica Militare
Paganella	pag	11.0; 46.2	2129	CM11 Kipp&Zonen	Aeronautica Militare
Aosta	aos	7.4; 45.7	583	CMP21 Kipp&Zonen	Arpa Valle D'Aosta

752

753

754 Table 3: Percentage of data in clear, contaminated and overcast conditions for all stations and
755 seasons, as well as for the whole year, estimated by CPP (Section 2.1).

Station	Winter [%]	Spring [%]	Summer [%]	Fall [%]	Year [%]
tra	48;23;29	/	82;15;03	38;39;23	60;24;16
csp	13;34;53	46;19;35	69;22;09	34;31;35	44;26;30
sml	33;31;36	37;40;23	62;31;07	41;37;22	44;34;20
pal	03;28;69	13;30;57	49;37;14	23;34;43	25;33;42
pdm	36;27;37	37;44;19	79;14;07	51;27;22	54;27;19
vdv	37;25;38	27;45;28	73;20;07	48;29;23	51;28;21
pis	34;22;45	38;33;29	77;16;07	44;29;27	52;24;24
cer	33;20;47	41;27;32	74;16;10	39;25;36	49;22;29
tri	20;21;59	31;29;40	64;24;12	34;23;43	42;24;34
cim	05;50;45	09;46;45	34;49;17	21;36;43	20;45;35
pag	23;22;55	39;27;34	45;38;17	27;31;42	35;31;34
aos	12;39;49	25;35;40	32;38;30	25;38;37	23;37;40

756

757

758 Table 4: rRMSE [%] for the MSG-GHI estimate computed for hourly and daily integrated GHI for
759 different seasons and stations. The first number in each cell is the rRMSE computed using hourly
760 data, the second number is the rRMSE computed for daily integrated GHI, the third number is the
761 rRMSE computed after the MOS correction for daily integrated GHI (see text for details).

Station	Winter [%]	Spring [%]	Summer [%]	Fall [%]	Year [%]
tra	30; 3; 3	/	11; 4; 4	27; 5; 6	18; 6; 7
csp	20; 5; 3	14; 4; 4	9; 4; 3	19; 3; 6	14; 6; 6
sml	27; 4; 4	21; 6; 6	14; 5; 4	23; 6; 7	19; 8; 8
pal	25; 4; 3	20; 5; 5	11; 4; 4	39; 4; 5	23; 7; 7

pdm	28; 3; 3	17; 5; 5	12; 4; 4	19; 6; 7	17; 7; 7
vdv	27; 3; 3	24; 5; 5	18; 6; 6	24; 4; 6	21; 8; 8
pis	26; 4; 3	22; 6; 5	16; 6; 5	20; 4; 5	19; 7; 7
cer	27; 4; 4	21; 6; 5	15; 6; 5	23; 3; 6	20; 8; 8
tri	34; 3; 3	28; 6; 6	22; 9; 8	25; 5; 7	26; 10; 10
cim	92; 18; 19	60; 24; 27	43; 23; 21	47; 13; 17	53; 27; 28
pag	57; 12; 10	35; 17; 16	38; 17; 17	43; 12; 11	40; 21; 20
aos	89; 7; 10	43; 12; 9	44; 12; 17	53; 6; 9	51; 15; 17

762

763

764 Table 5: rRMSE [%] for the RAMS-GHI one-day forecast computed for hourly and daily integrated
765 GHI for different seasons and stations. The first number in each cell is the rRMSE computed using
766 hourly data, the second number is the rRMSE computed for daily integrated GHI, the third number
767 is the rRMSE computed after the MOS correction for daily integrated GHI (see text for details).

Station	Winter [%]	Spring [%]	Summer [%]	Fall [%]	Year [%]
tra	58; 12; 8	/	20; 12; 10	49; 17; 17	33; 21; 19
csp	43; 12; 9	38; 23; 19	19; 11; 10	42; 15; 16	31; 22; 19
sml	57; 14; 11	47; 25; 19	26; 16; 12	42; 15; 13	38; 27; 21
pal	58; 16; 9	54; 25; 20	27; 18; 16	47; 16; 16	41; 28; 25
pdm	60; 14; 11	48; 28; 21	25; 15; 14	40; 12; 13	37; 27; 22
vdv	66; 14; 10	57; 28; 19	32; 19; 16	49; 14; 14	42; 29; 23
pis	68; 15; 10	56; 28; 21	32; 22; 18	51; 17; 17	45; 30; 25
cer	68; 13; 10	52; 26; 19	34; 20; 16	53; 14; 13	44; 29; 23
tri	97; 16; 11	63; 26; 19	44; 26; 20	58; 16; 15	53; 35; 27
cim	117; 22; 22	96; 44; 44	60; 39; 30	74; 24; 24	75; 48; 44
pag	86; 15; 10	77; 50; 28	66; 44; 26	79; 30; 30	72; 56; 36
aos	113; 17; 17	78; 49; 25	71; 48; 43	84; 23; 23	81; 60; 42

768

769

770

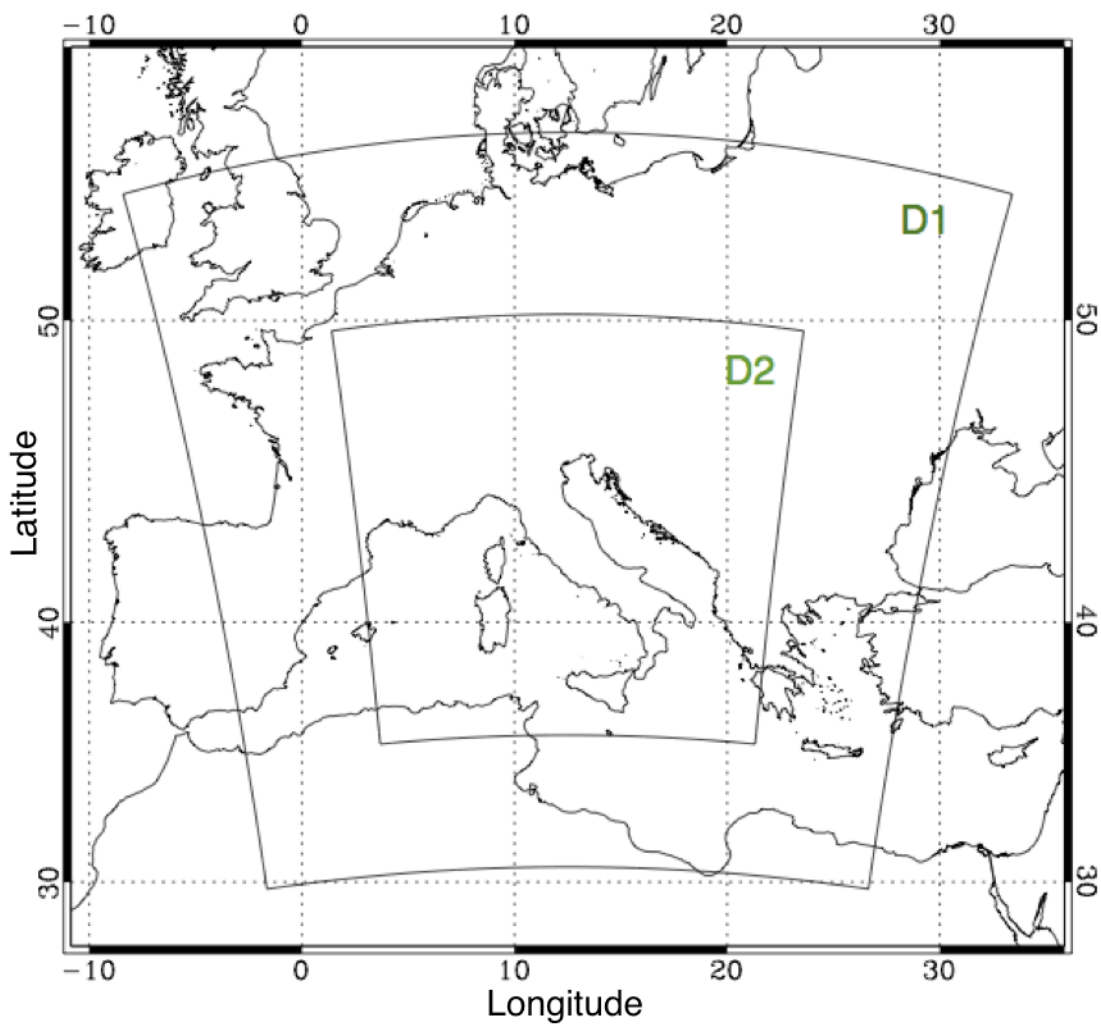
771

772 Table 6: RMSE [W/m^2] for the RAMS-GHI one-day hourly forecast (first number in each cell),
773 one-day persistence hourly forecast (second number in each cell) and RAMS-GHI one-day hourly
774 forecast after the MOS application for different seasons and stations (third number in each cell, see
775 text for details). Bold style shows the cases when the RAMS-GHI one-day hourly forecast has a
776 worse performance compared to the one-day persistence hourly forecast.

Station	Winter [W/m^2]	Spring [W/m^2]	Summer [W/m^2]	Fall [W/m^2]	Year [W/m^2]
tra	149 ; 120; 130	/	111; 136; 104	177 ; 162; 163	152; 190; 139
csp	137; 169; 126	199; 218; 184	107; 168; 102	168; 191; 157	161; 204; 148

sml	151; 170; 133	218; 275; 200	142; 178; 128	159; 186; 147	178; 236; 160
pal	138; 177; 125	232; 257; 212	145; 181; 141	173; 192; 161	186; 229; 171
pdm	140; 151; 123	226; 231; 206	133; 172; 132	144; 167; 139	176; 209; 161
vdv	138; 161; 115	230; 238; 196	168; 189; 158	158; 170; 140	182; 209; 159
pis	125 ; 119; 104	227 ; 223; 200	165; 180; 153	163; 174; 150	188; 216; 166
cer	120 ; 118; 100	204; 241; 182	170; 206; 158	149 ; 147; 139	178; 220; 157
tri	131 ; 77; 181	207 ; 195; 181	206; 223; 189	147 ; 142; 134	190; 220; 166
cim	158 ; 145; 160	288; 289; 288	253; 274; 220	199 ; 193; 183	253; 293; 238
pag	148 ; 95; 114	318 ; 266; 239	304 ; 291; 255	224 ; 156; 183	286 ; 276; 221
aos	172 ; 99; 148	341 ; 234; 256	326; 347; 281	200 ; 126; 176	287; 294; 229

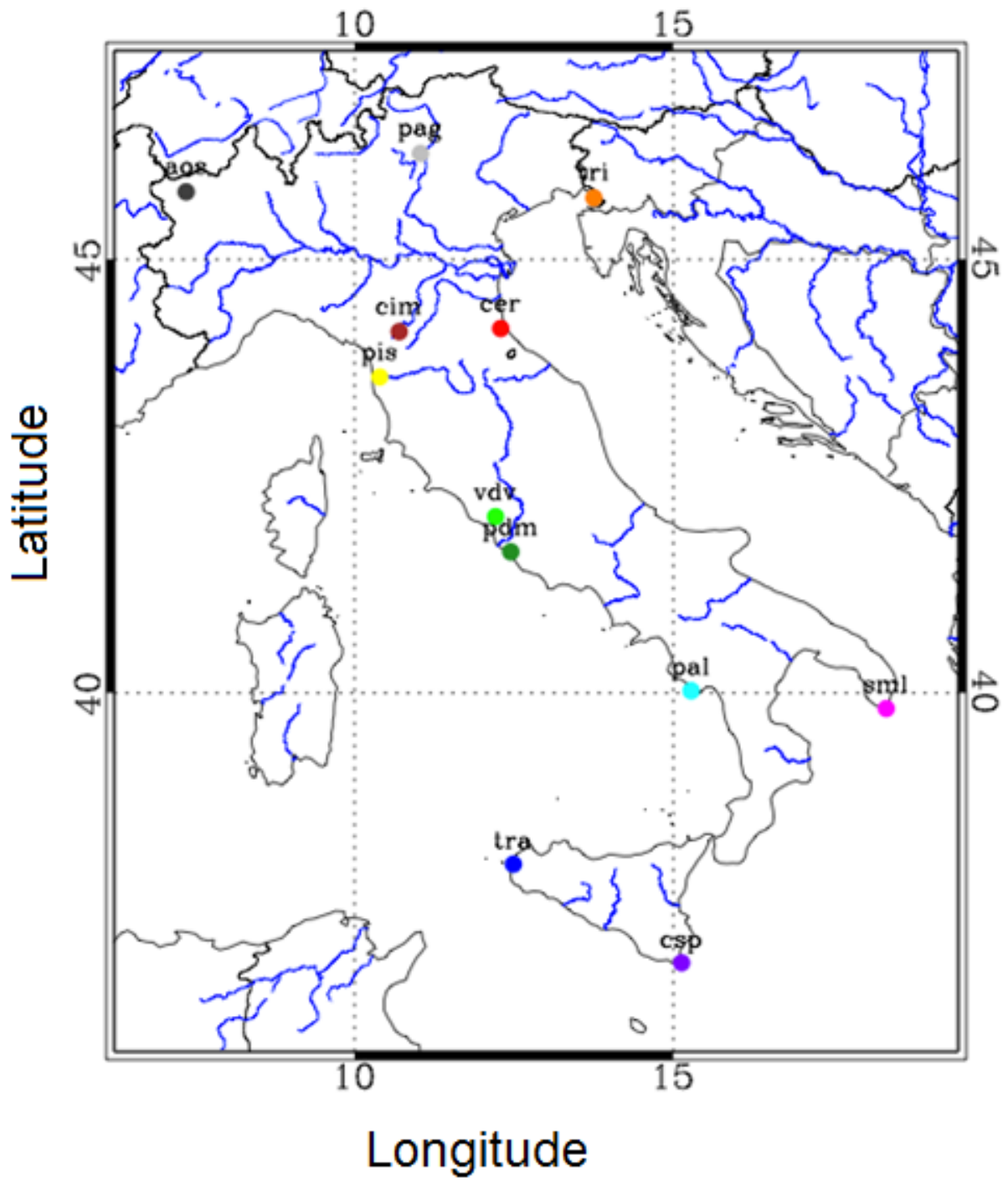
777



778

779 **Figure 1:** Model domains. The second domain has 4 km horizontal resolution and it is nested in the
780 first domain, at 12 km horizontal resolution, using one-way nesting.

781



782

783 **Figure 2:** Stations distribution over the Italian territory.

784

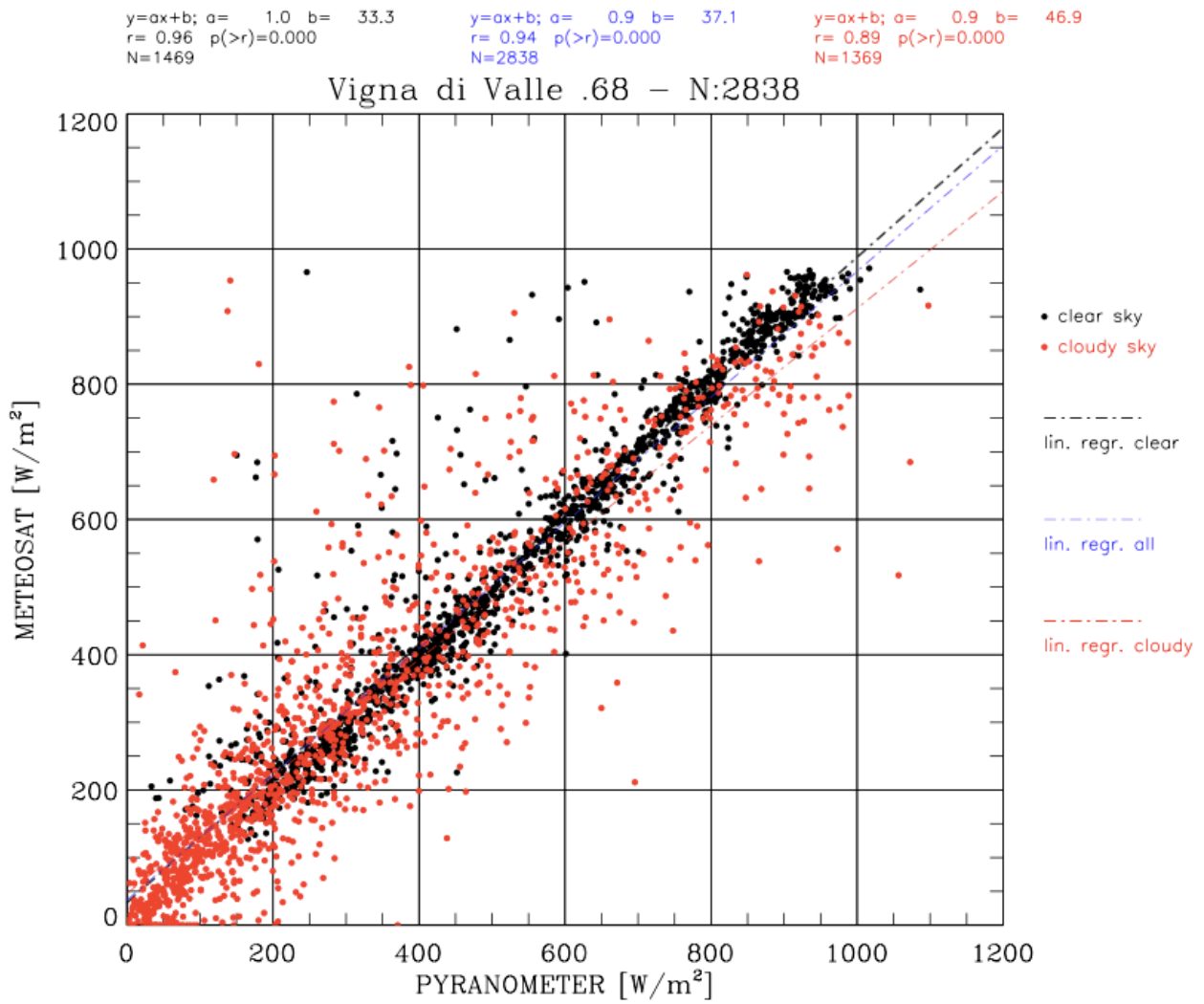
785

786

787

788 a)

789



790

791

792

793

794

795

796

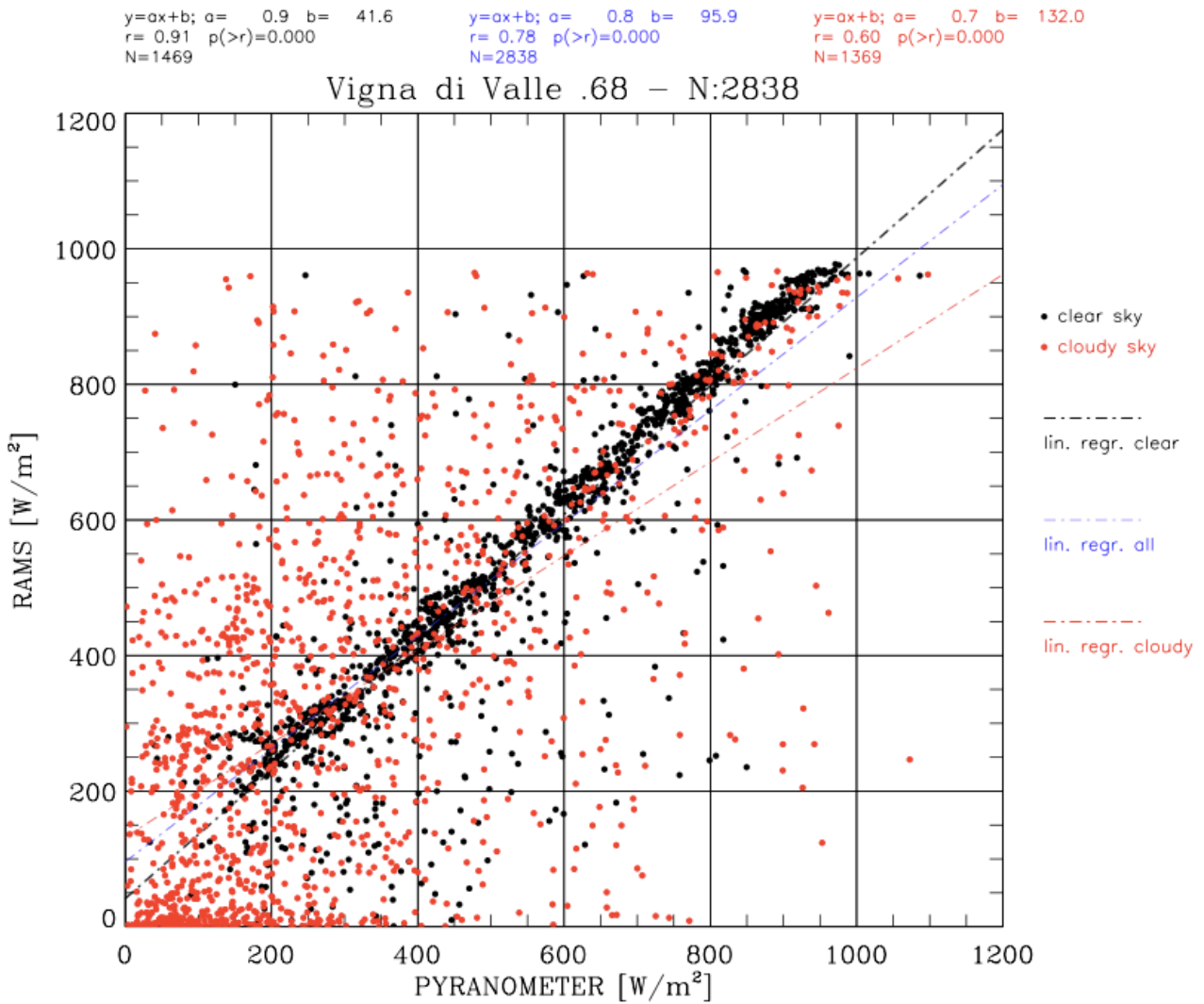
797

798

799

800

801 **b)**



802

803

804 Figure 3: a) scatter plot of the GHI for the pyranometer (x -axis) and MSG (y -axis) hourly data. The
805 black dots are for clear sky conditions while the red dots are for both contaminated and overcast
806 skies; b) as in a) for the RAMS one-day hourly forecast. Regression lines are shown in their
807 respective colours (blue is for all data, i.e. both clear and cloudy conditions).

808

809

810

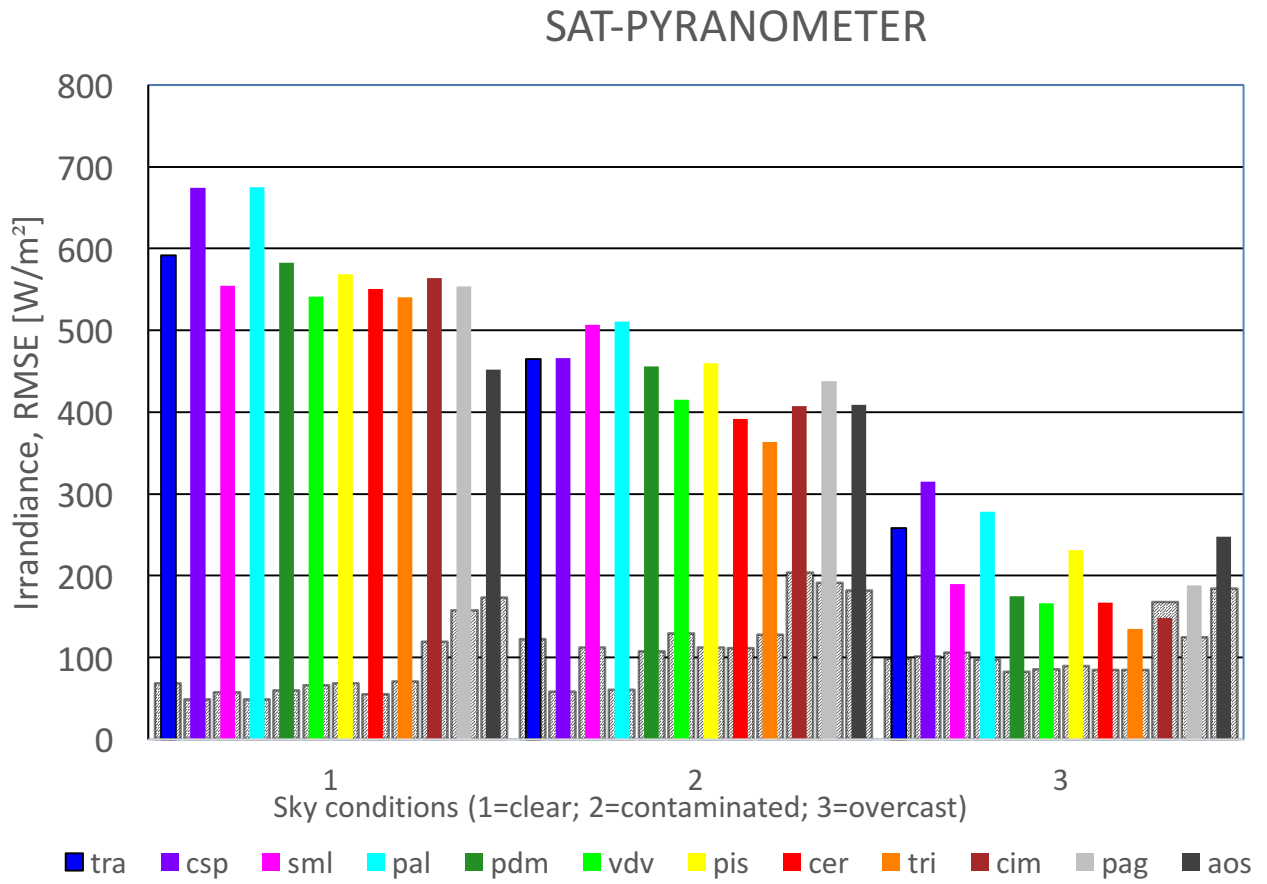
811

812

813

814

815 a)



816

817

818

819

820

821

822

823

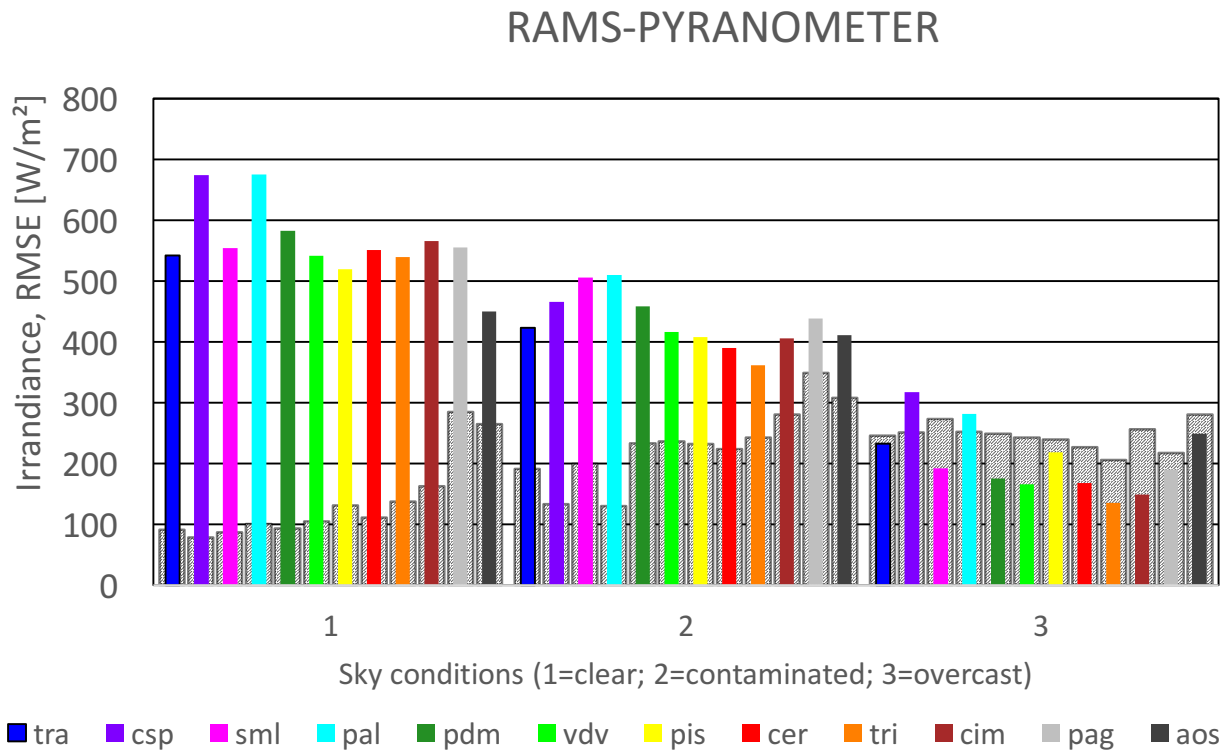
824

825

826

827

828 b)



829

830 Figure 4: a) Mean irradiance (coloured bars) and RMSE (grey bars) for different sky conditions:
831 clear (1), contaminated (2) and overcast (3) for the MSG-GHI estimate. The figure has been derived
832 from the hourly data of pyranometers and MSG-GHI estimate. The RMSE is shown with the same
833 scale as the mean irradiance; b) As in a) for the RAMS-GHI one-day hourly forecast.

834

835

836

837

838

839

840

841

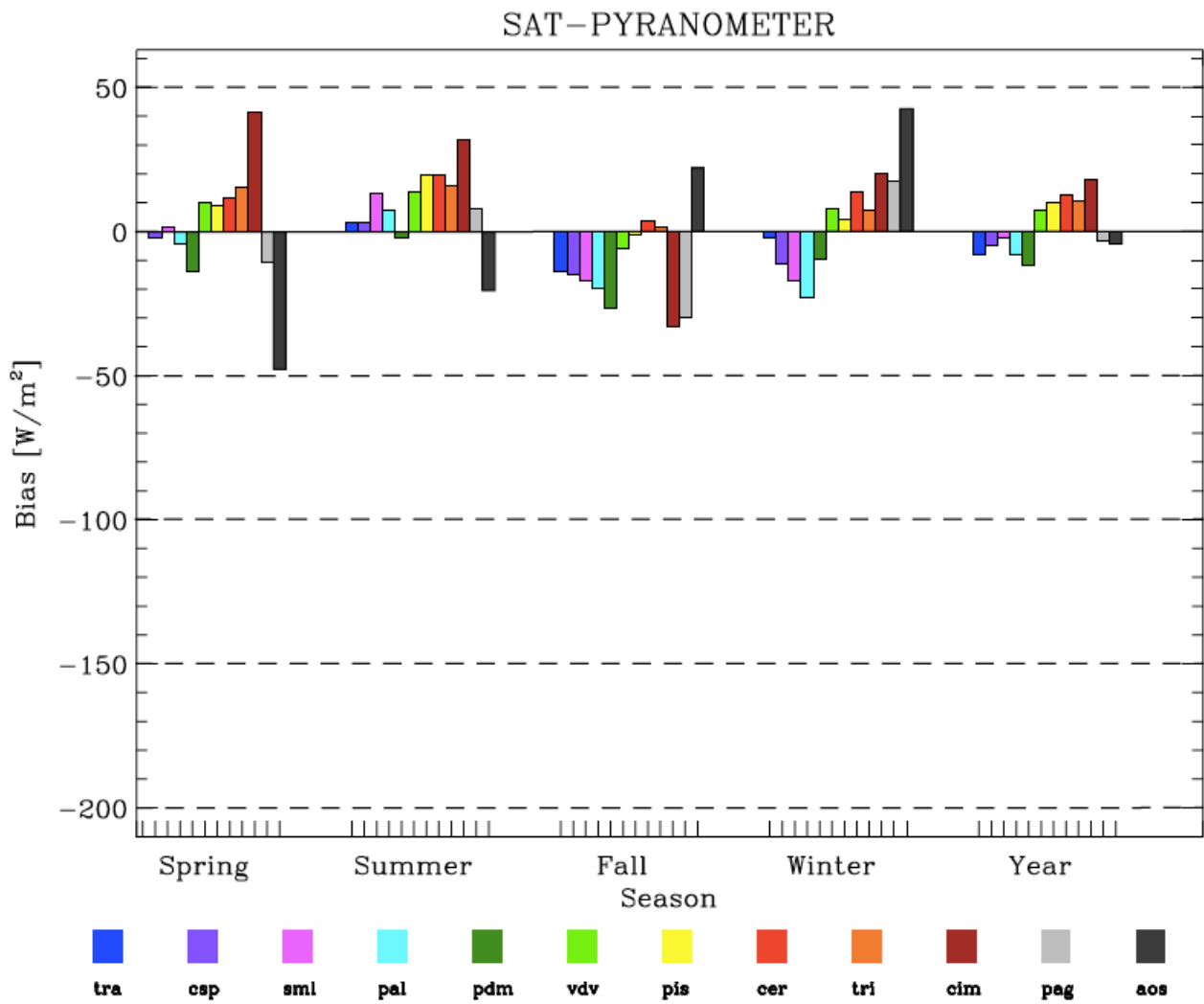
842

843

844

845

846 a)



847

848

849

850

851

852

853

854

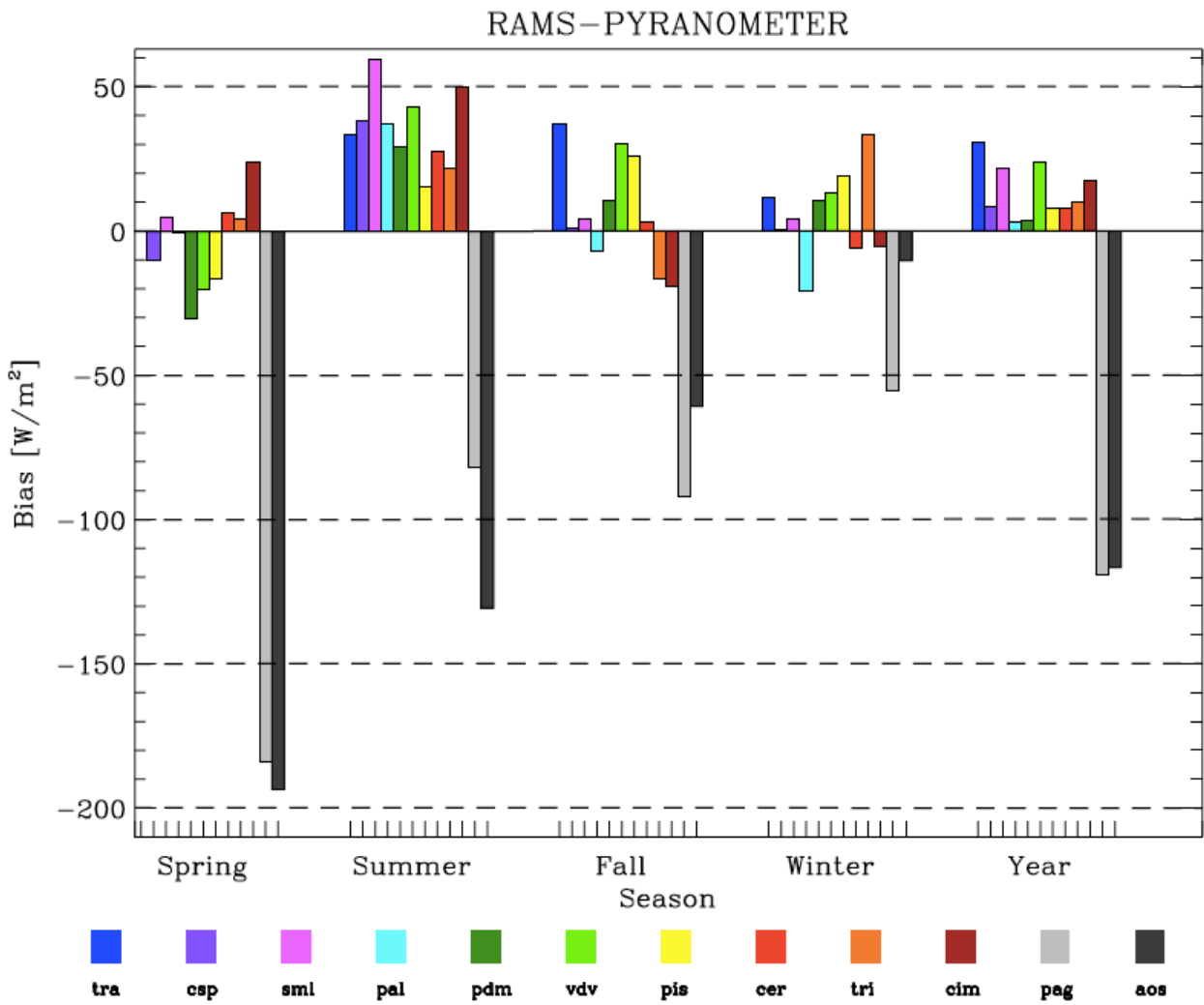
855

856

857

858

859 b)



860

861 Figure 5: a) MBE for the MSG-GHI for the different stations and seasons as well as for the whole
862 year. The figure has been derived from the hourly data of pyranometers and MSG-GHI estimate; b)
863 As in Figure 5a for the RAMS forecast.

864

865

866

867

868

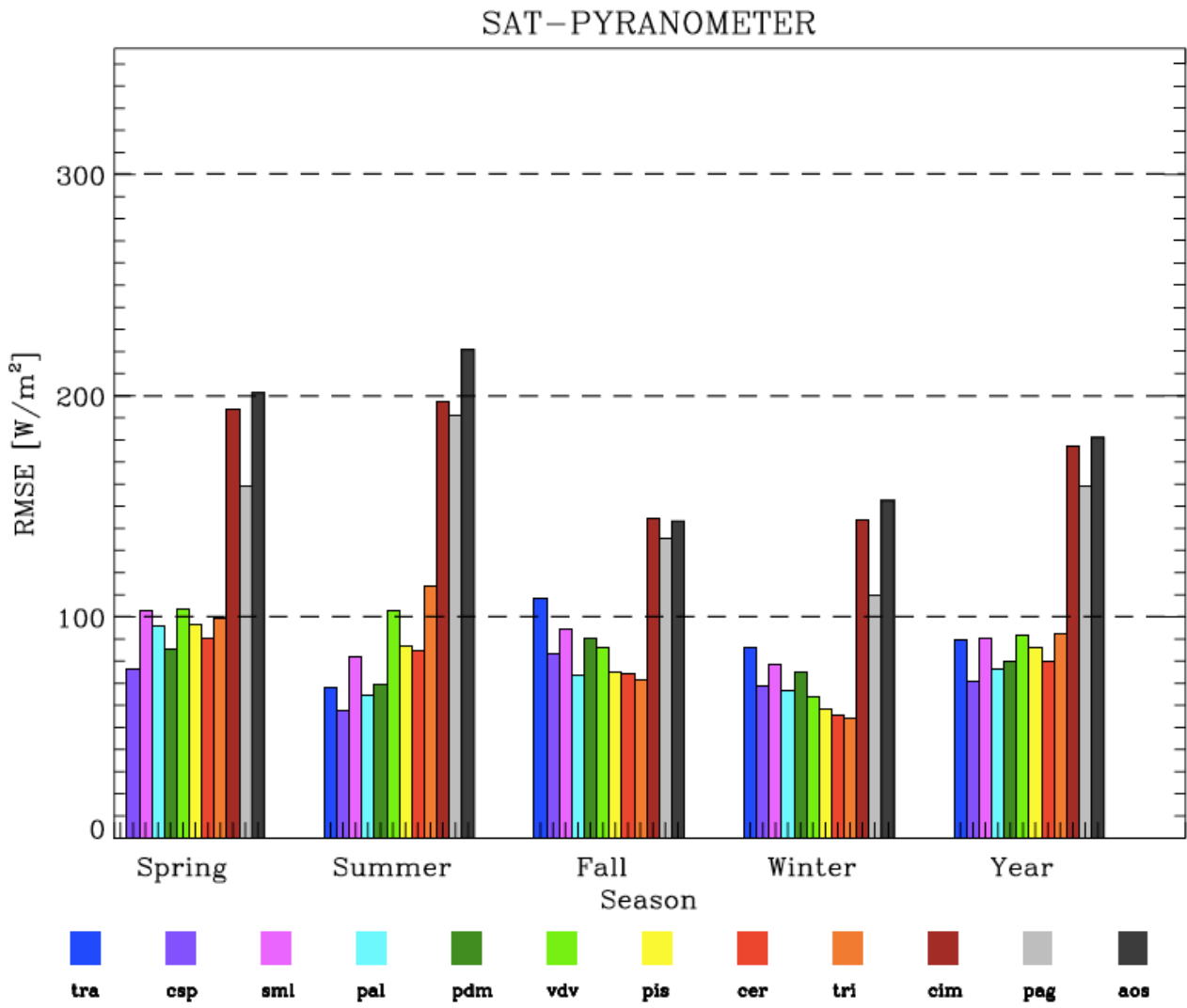
869

870

871

872

873 a)



874

875

876

877

878

879

880

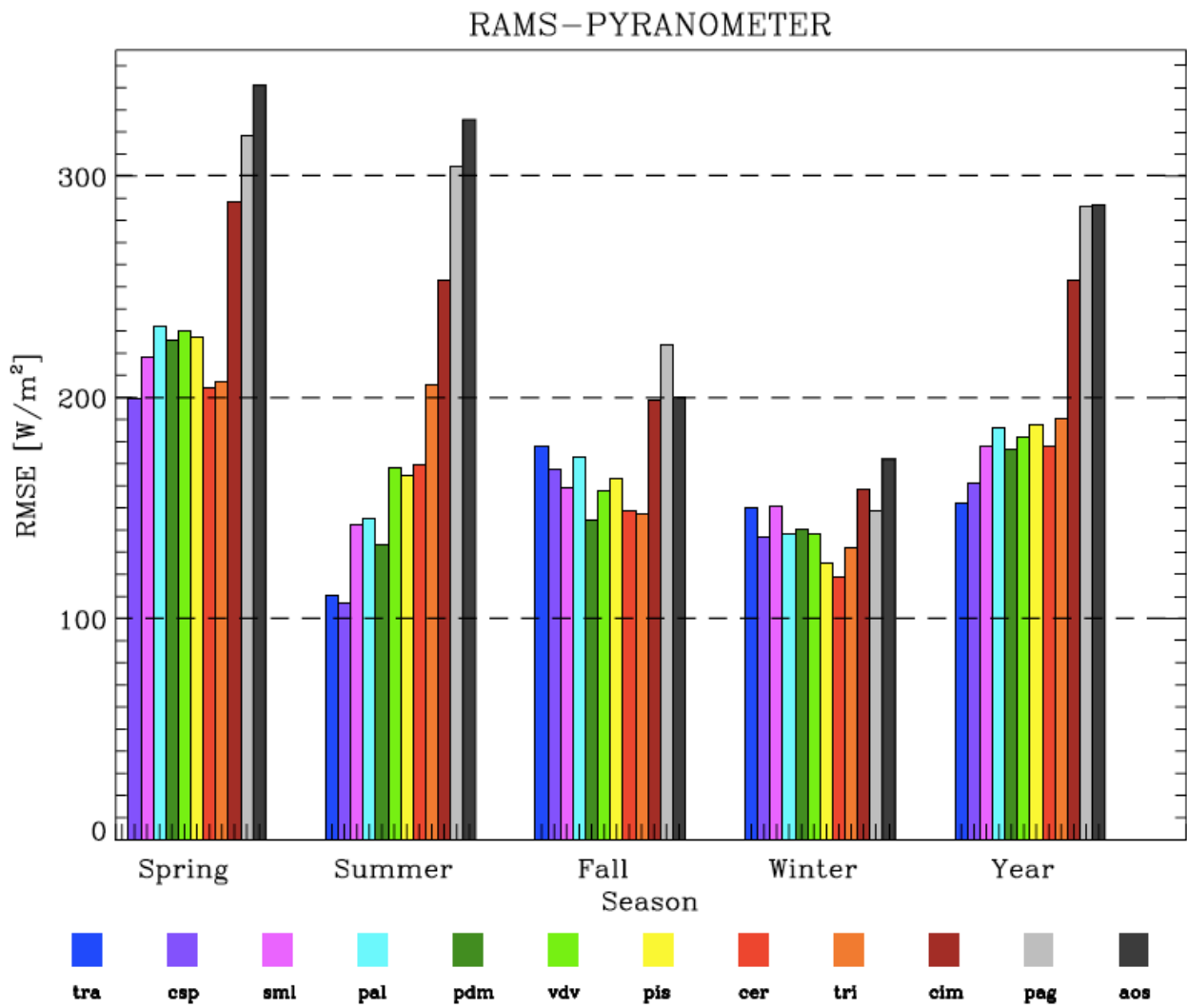
881

882

883

884

885 b)



886

887 Figure 6: a) RMSE for the MSG-GHI for the different stations and seasons as well as for the whole
888 year. The figure has been derived from the hourly data of pyranometers and MSG-GHI estimate; b)
889 As in a) for the RAMS forecast.

890

891

892

893

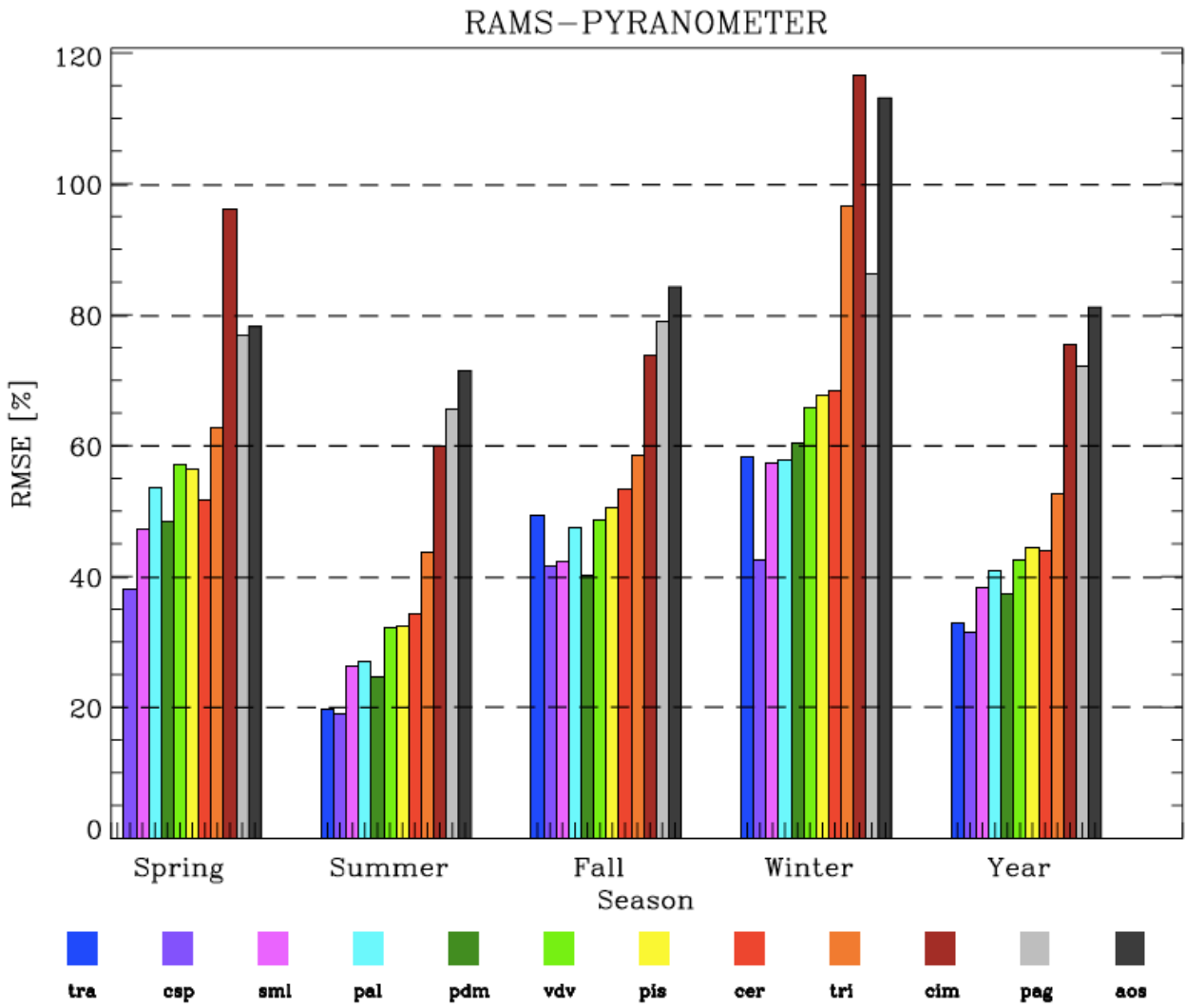
894

895

896

897

898 a)



899

900

901

902

903

904

905

906

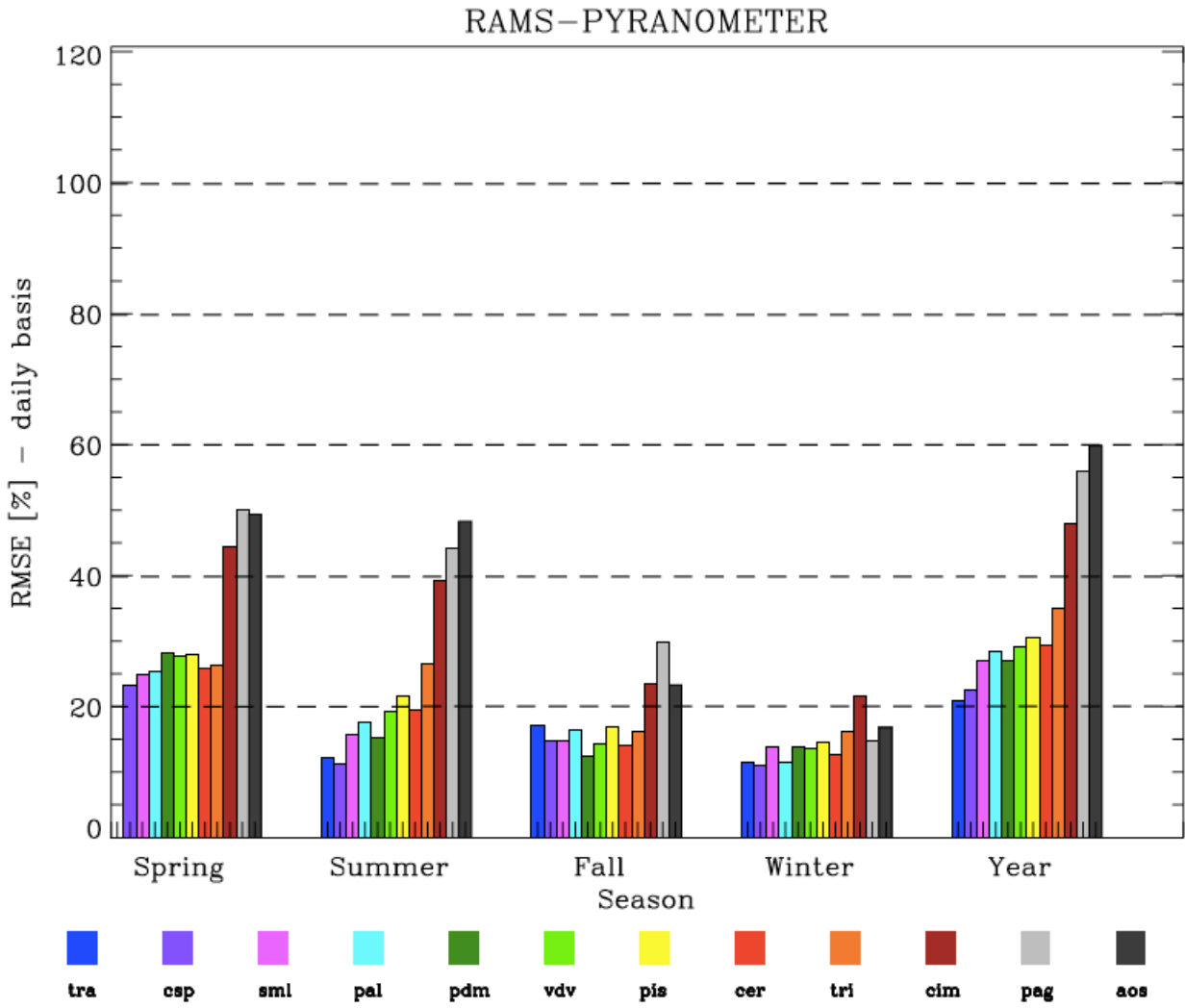
907

908

909

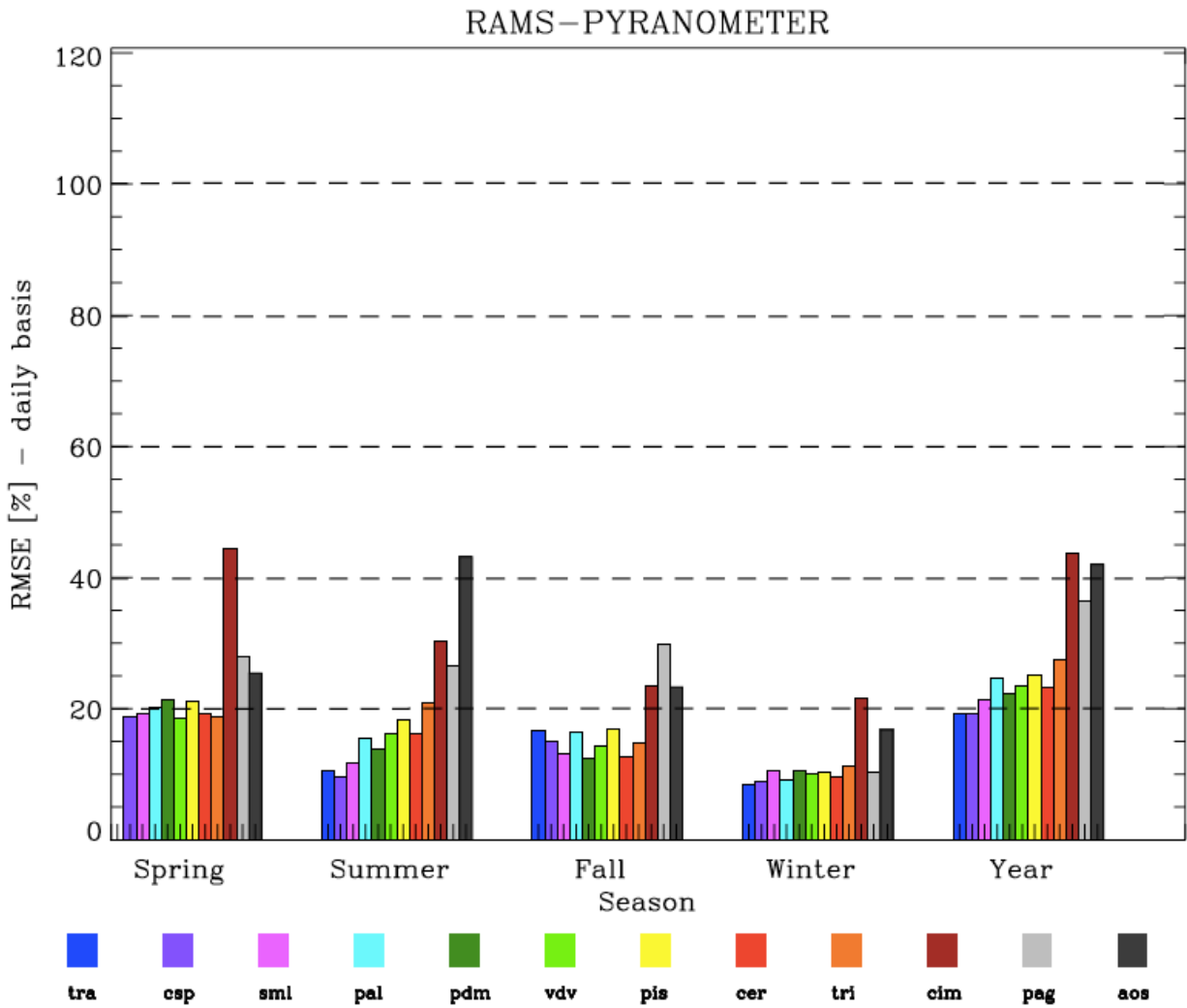
910

911 **b)**



912

913 c)



914

915

916 Figure 7: a) rRMSE computed for different seasons and stations, as well as for the whole year, for
 917 the RAMS-GHI one-day hourly forecast; b) as in a) for daily integrated GHI; c) as in b) after the
 918 MOS correction to the model output.

919